

Galaxy formation and evolution – I. The Padua TREE-SPH code (PD-SPH)

Giovanni Carraro,^{1,2} Cesario Lia² and Cesare Chiosi¹

¹*Dipartimento di Astronomia, Università di Padova, Vicolo dell'Osservatorio 5, I-35022 Padova, Italy*

²*SISSA-ISAS, via Beirut 2–4, I-34013 Trieste, Italy*

Accepted 1998 February 2. Received 1998 January 19; in original form 1997 May 21

ABSTRACT

In this paper we report on PD-SPH, the new TREE-SPH code developed in Padua. The main features of the code are described and the results of a new and independent series of 1D and 3D tests are shown. The paper is mainly dedicated to the presentation of the code and to the critical discussion of its performance. In particular, great attention is devoted to the convergency analysis. The code is highly adaptive in space and time by means of individual smoothing lengths and individual time-steps. At present it contains both dark and baryonic matter, this latter in the form of gas and stars, cooling, thermal conduction, star formation, feedback from Type I and II supernovae, stellar winds, and ultraviolet flux from massive stars, and finally chemical enrichment. New cooling rates that depend on the metal abundance of the interstellar medium are employed, and the differences with respect to the standard ones are outlined. Finally, we show the simulation of the dynamical and chemical evolution of a disc-like galaxy with and without feedback. The code is suitably designed to study in a global fashion the problem of formation and evolution of elliptical galaxies, and in particular to feed a spectrophotometric code from which the integrated spectra, magnitudes and colours (together with their spatial gradients) can be derived.

Key words: hydrodynamics – methods: numerical – galaxies: evolution – galaxies: formation.

1 INTRODUCTION

The conventional picture of star formation in elliptical galaxies is one in which the galaxies and their stellar content formed early in the Universe and have evolved quiescently ever since. This view is supported by the apparent uniformity of elliptical galaxies in photometric and chemical appearance (cf. Matteucci 1997 for a recent review) and the existence of scaling relations, e.g. the Fundamental Plane (cf. Bender 1997). In contrast, the close scrutiny of nearby elliptical galaxies makes evident a large variety of morphological and kinematic peculiarities and the occurrence of star formation in the recent past (Schweizer & Seitzer 1992). All this leads to a different picture in which elliptical galaxies are formed by mergers and/or accretion of smaller units over a time-scale comparable to the Hubble time. Furthermore, strong evolution in the population of early-type galaxies has been reported by Kauffmann, Charlot & White (1996), which has been considered to support the

hierarchical galaxy-formation model (Kauffmann, White & Guiderdoni 1993; Baugh, Cole & Frenk 1996).

Tracing back the formation mechanism of elliptical galaxies from the bulk of their chemospectrophotometric properties is a cumbersome affair because studies of stellar populations in integrated light reveal only luminosity-weighted ages and metallicities, and are ultimately unable to distinguish between episodic (perhaps recurrent) and monolithic histories of star formation, and between star-formation histories in isolation or interaction. Nowadays, most of the properties of elliptical galaxies have been studied with sophisticated chemospectrophotometric models in which the dynamical process of galaxy formation is reduced to assuming either the closed box or infall scheme and a suitable law of star formation (Arimoto & Yoshii 1987, 1989; Bruzual & Charlot 1993; Bressan, Chiosi & Fagotto 1994; Worthey 1994; Tantalo et al. 1996; Bressan, Chiosi & Tantalo 1996; Gibson 1996a,b,c, 1997; Gibson & Matteucci 1997; Tantalo et al. 1997). In contrast, the

highly sophisticated dynamical models of galaxy formation (Hernquist & Katz 1989; Davis et al. 1992; Katz 1992; Steinmetz & Müller 1993; Navarro & White 1993; Nelson & Papaloizou 1994; Katz, Weinberg & Hernquist 1996; Steinmetz & Müller 1995; Heihnel, Steinmetz & Rauch 1996a, b; Navarro, Frenk & White 1996; Steinmetz 1996a, b and references; Navarro & Steinmetz 1997), owing to the complexity of the problem, are still unable to make detailed predictions about the chemospectrophotometric properties of the galaxies in question. Attempts to bridge the two aspects of the same problem have been made by Theis, Burkert & Hensler (1992 and references) and most recently by Conrado, Steinmetz & Fritze-v-Alvensleben (in preparation).

This paper is the first of a series dedicated to the study of this complex problem in a self-consistent fashion, in which the formation and evolution of galaxies, together with their chemospectrophotometric properties, stem from a unique model able to predict a number of observable quantities to be compared with real data. The project aims to build dynamical models of disc-like and elliptical galaxies by means of the SPH (Smoothed Particle Hydrodynamics) technique, in which the effects of different initial conditions and basic physical processes, such as star formation, heating of the gas by various mechanisms (supernova explosions, stellar winds, UV fluxes), cooling of the gas by radiative atomic and molecular agents, interplay between dynamics and thermodynamics (feedback) and chemical enrichment of the interstellar medium are taken into account. The models allow for the presence of dark matter and the effect of this on the gravitational field, which is described using a Barnes & Hut (1986) tree-code. The rates of star formation and chemical enrichment as a function of space and time resulting from the dynamical models are meant to feed chemospectrophotometric models that should provide the kind of data (luminosities, integrated spectral energy distributions, broad-band colours, line-strength indices, etc.) to be compared with real observations for nearby and high-redshift galaxies.

In this paper we present the first step toward this articulated analysis of the problem, i.e. the tool to construct dynamical models, and describe in some detail the numerical algorithm and the key physical ingredients. The dynamical models are based on the SPH technique, one of the most popular and efficient tools of modern studies of numerical hydrodynamics, and in the astrophysical context of structures and galaxy formation. In the following we will refer to the SPH code we have developed as the Padua SPH (PD-SPH).

When SPH is coupled with an efficient scheme to compute gravity (like tree-codes), it becomes a powerful tool with which to investigate physical situations of enormous complexity such as, for instance, the formation and evolution of a galaxy (in the isolation picture) and/or the interaction-merging of galaxies (in the hierarchical scenario). The Lagrangian nature of the method allows us to follow the evolution of physical quantities at all scales, provided that sufficient resolution is ensured.

The plan of the paper is as follows. Section 2 gives a detailed description of the code. Section 3 discusses tests in one dimension, i.e. the results for the Riemann problem and the convergency analysis, whereas Section 4 contains tests performed in three dimensions. Section 5 presents the first

astrophysical application, i.e. the collapse of a galaxy made of gas and dark matter in presence of initial solid-body rotation. Section 6 thoroughly presents non-adiabatic processes, such as thermal conduction, radiative cooling and heating by Type I and II supernova explosions, and stellar winds and ultraviolet radiation from massive stars that have been used as source or sink of energy in our models. We adopt cooling rates that take the effect of metallicity into account. In Section 7 we describe the results obtained from our cooling prescription and compare them with those from metal-independent cooling rates. Section 8 describes our prescriptions for the star-formation rate and feedback (rate of energy input from supernovae, stellar wind and UV emission), and the rate of chemical enrichment. Section 9 presents the results for two disc-like galaxies: the first case is with no feedback of any type, whereas the second case is with feedback. These models are not meant to represent real galaxies, first because the initial conditions are not derived from a cosmological context, and secondly because the total number of particles is small owing to limitations in the computing facilities. The models are indeed meant to test the code response to various physical inputs. Nevertheless, despite the present limitations, the results are very promising. Finally, Section 10 presents some concluding remarks and outlines the perspectives of future studies.

2 THE PD-SPH CODE

PD-SPH is a TREE-SPH code, written in FORTRAN 90 (cf. Carraro 1995 Lia 1996), conceptually similar to those described by Hernquist & Katz (1989) and Nelson & Papaloizou (1994). A 1D version of the SPH code is in parallel form, and it has already been tested on the Cray T3D parallel computer hosted by CINECA (Benincà & Carraro 1995).

Schematically, PD-SPH uses SPH to solve the equations of motion for the gas component, and the Barnes & Hut (1986) octo-tree to compute the gravitational interactions. In this section we describe in some detail the structure of the code and its basic ingredients.

It is widely known that SPH is a method standing on two basic ingredients: an interpolation using a kernel, and a Monte Carlo evaluation of the physical quantities. All relevant variables are interpolated in the following way:

$$\langle f(\mathbf{r}) \rangle = \int W(\mathbf{r} - \mathbf{r}', h) f(\mathbf{r}') d\mathbf{r}', \quad (1)$$

where the integral is extended over the whole space and W is a function generally referred to as the interpolating kernel; h is the *smoothing length* determining the spatial region within which variables are smoothed, and governing the spatial resolution of the method.

The kernel is a spherically symmetric function strongly peaked at $\mathbf{r} = \mathbf{r}'$. It is easy to prove (Benz 1990) that these properties make SPH a second-order technique, in which the estimate of any function is given by

$$\langle f(\mathbf{r}) \rangle = f(\mathbf{r}) + c(\nabla^2 f) h^2 + O(h^3). \quad (2)$$

This estimate is made in Lagrangian formalism, summing up the contributions of all the particles within $2 \times h$, which represent the so-called neighbours.

2.1 Interpolating kernel

Three types of kernel can basically be found in the literature: exponential, Gaussian and spline; see Benz (1990) for more details. We have adopted the spline kernel of Monaghan & Lattanzio (1985):

$$W(r, h) = \frac{1}{\pi h^3} \begin{cases} 1 - \frac{3}{2}u^2 + \frac{3}{4}u^3, & \text{if } 0 \leq u \leq 1; \\ \frac{1}{4}(2-u)^3, & \text{if } 1 \leq u \leq 2; \\ 0 & \text{otherwise,} \end{cases} \quad (3)$$

and the super-Gaussian kernel in Gingold & Monaghan (1983):

$$W(r, h) = \frac{1}{\pi^{3/2} h^3} \left(\frac{5}{2} - u \right) \exp(-u^2), \quad (4)$$

where $u = |r|/h$.

The super-Gaussian kernel is built up by forcing the second-order term in equation (2) to be zero. It can be shown that this kernel corresponds to a fourth-order interpolation. This kernel becomes negative for $r/h > \sqrt{5/2}$ (Benz 1990) and does not find an immediate physical interpretation.

Moreover, while the spline kernel is defined on a compact support, the super-Gaussian kernel needs an artificial cut-off to limit the number of neighbours utilized in the estimate of the physical quantities. First we checked both kernels (see Section 3 for details) and finally we adopted the spline kernel. In our code it is stored as a look-up table.

2.2 Evolution of the smoothing length and the search of neighbour particles

In SPH the spatial resolution is fixed by the smoothing length h . In our code h is kept variable both in space and time according to Benz (1990):

$$\frac{dh}{dt} = -\frac{1}{3} \frac{h_i}{\rho_i} \frac{d\rho_i}{dt} = \frac{1}{3} h \nabla \mathbf{v}. \quad (5)$$

This equation is added to the set of equations to be solved at any time-step. The main drawback of this approach is that in situations in which strong density gradients are present it is not possible to keep under control the number of neighbours. Typically this number should be about 40–50 (Steinmetz & Müller 1993).

One possible solution is to artificially increase or decrease h in order to keep the neighbour number fixed, but this involves several iterations if – as in our case – the tree-code is used to look for neighbours. As a consequence of this, the computational time often becomes unacceptably long.

To cope with this difficulty, we have decided to maintain the above scheme when the neighbour number is lower than 40, and switch to the Nelson & Papaloizou (1994) formalism when the neighbour number is greater than 80. Accordingly the new smoothing length h is

$$h_i = \frac{1}{N_{\text{far}}} \sum_{n=1}^{N_{\text{far}}} \frac{1}{2} |\mathbf{r}_i - \mathbf{r}_n| \quad (6)$$

where N_{far} are the n most distant nearest neighbours. We assume $N_{\text{far}} = 10$.

There is another drawback in the Benz (1990) formalism that deserves some attention. The space–time variation of the smoothing length generally hampers the strict conservation of energy when terms involving the space derivatives of h are not included. ∇h terms are essentially small corrections (cf. the thorough discussion by Nelson & Papaloizou 1994), which do not significantly improve upon the conservation of energy.

Moreover the momentum conservation has been secured at an acceptable level of confidence also by symmetrizing the search of the nearest neighbours. In brief, a candidate particle i is considered as a neighbour of j if the following conditions are met:

$$|\mathbf{r}_i - \mathbf{r}_j| < 2 \cdot h_i$$

or

$$|\mathbf{r}_i - \mathbf{r}_j| < 2 \cdot h_j$$

2.3 Hydrodynamical equations

In PD-SPH, the particle forces and the specific energy are computed by means of the following equations

$$\begin{aligned} \frac{d\mathbf{v}_i}{dt} = & - \sum_{j=1}^N \left(\frac{\sqrt{P_i P_j}}{\rho_i \rho_j} + \Pi_{ij} \right) \\ & \times \frac{1}{2} [\nabla_i W(r_{ij}, h_i) + \nabla_i W(r_{ij}, h_j)] \end{aligned} \quad (7)$$

and

$$\begin{aligned} \frac{du_i}{dt} = & \sum_{j=1}^N m_j \left(\frac{\sqrt{P_i P_j}}{\rho_i \rho_j} + \frac{1}{2} \Pi_{ij} \right) \mathbf{v}_{ij} \\ & \times \frac{1}{2} [\nabla_i W(r_{ij}, h_i) + \nabla_i W(r_{ij}, h_j)] + \Gamma_R - \frac{\Lambda_C}{\rho}, \end{aligned} \quad (8)$$

in which we adopt the arithmetic mean for the pressure gradient as in Hernquist & Katz (1989). Furthermore, in equation (8) the first term represents the heating rate of mechanical nature (it is indicated in short as Γ_M), the second term Γ_R is the total heating rate from all sources apart from the mechanical ones, and the third term Λ_C/ρ is the total cooling rate caused by many physical agents. These latter two will be discussed below in more detail. In the above equations $\mathbf{v}_{ij} = \mathbf{v}_i - \mathbf{v}_j$, and Π_{ij} is the viscosity tensor defined as

$$\Pi_{ij} = \begin{cases} \frac{-\alpha c_{ij} \mu_{ij} + \beta \mu_{ij}^2}{\rho_{ij}}, & \text{if } (\mathbf{v}_i - \mathbf{v}_j) \cdot (\mathbf{r}_i - \mathbf{r}_j) > 0 \\ 0 & \text{otherwise,} \end{cases} \quad (9)$$

where

$$\mu_{ij} = \frac{h_{ij} (\mathbf{v}_i - \mathbf{v}_j) \cdot (\mathbf{r}_i - \mathbf{r}_j)}{|\mathbf{r}_i - \mathbf{r}_j|^2 + \epsilon h_{ij}^2}. \quad (10)$$

Here $c_{ij}=0.5(c_i+c_j)$ is the sound speed, $h_{ij}=0.5(h_i+h_j)$, and α and β are the viscosity parameters, usually set to 1.0 and 2.0, respectively. The factor ϵ is fixed to 0.01 and is meant to avoid divergence.

As amply discussed in Navarro & Steinmetz (1997) this formulation has the disadvantage of not vanishing in the case of shear-dominated flows, when $\nabla \cdot \mathbf{v}=0$ and $\nabla \times \mathbf{v} \neq 0$. In such a case, spurious shear viscosity can develop, mainly in simulations involving a small number of particles. To reduce the shear component we adopt the Balsara (1995) formulation of the viscosity tensor,

$$\tilde{\Pi} = \Pi_{ij} \times \frac{f_i + f_j}{2}, \quad (11)$$

where f_i is a suitable function defined as

$$f_i = \frac{|\langle \nabla \cdot \mathbf{v} \rangle_i|}{|\langle \nabla \cdot \mathbf{v} \rangle_i| + |\langle \nabla \times \mathbf{v} \rangle_i| + \eta c_i/h_i}, \quad (12)$$

and $\eta \approx 10^{-4}$ is a parameter meant to prevent numerical divergences.

2.4 Time integration and stability criteria

Particle positions and velocities are updated, as in Hernquist & Katz (1989), using the leapfrog integrator and the multiple time-step scheme. The integration is of the second order in time, and proceeds as in the classical scheme.

Firstly an estimate of the velocity $\tilde{\mathbf{v}}_i^{n+1/2}$ is obtained from

$$\tilde{\mathbf{v}}_i^{n+1/2} = \mathbf{v}_{ni} + 0.5 \Delta t_i \mathbf{a}_i^{n-1/2}. \quad (13)$$

This is used to compute time-centred accelerations, $\mathbf{a}_i^{n+1/2}$, from which particle velocities and positions are updated:

$$\mathbf{v}_i^{n+1} = \mathbf{v}_i^n + \Delta t_i \mathbf{a}_i^{n+1/2} \quad (14)$$

$$\mathbf{r}_i^{n+1/2} = \mathbf{r}_i^{n-1/2} + \Delta t_i \mathbf{v}_i^n. \quad (15)$$

The energy equation is explicitly solved, unless sink or source terms are present, and particle energies are advanced in the same manner as positions.

Time-steps are calculated according to the Courant condition

$$\Delta t_{C,i} = \mathcal{C} \frac{h_i}{h_i |\nabla \cdot \mathbf{v}_i| + c_i + 1.2 (\alpha c_i + \beta \max_j |\mu_{ij}|)}, \quad (16)$$

where $\mathcal{C} \approx 0.3$.

In the presence of gravity, a more stringent condition on the time-steps is required. According to Katz, Weinberg & Hernquist (1996), the additional criterion that has to be satisfied is

$$\Delta t_{G,i} = \eta \cdot \min \left[\frac{\eta \epsilon}{|\mathbf{v}|}, \left(\frac{\epsilon}{|\mathbf{a}|} \right)^{1/2} \right], \quad (17)$$

where ϵ is the gravitational softening parameter and η is another parameter usually set to 0.5. The final time-step to be adopted is the smallest of the two:

$$\Delta t_i = \min (\Delta t_{C,i}, \Delta t_{G,i}). \quad (18)$$

While the use of the multiple time-step scheme may significantly speed up the code (Steinmetz 1995), sometimes the interpolations of non-active particles may affect the energy conservation (see Section 4).

3 1D NUMERICAL TESTS

The classical 1D test to which SPH codes are compared is the Riemann shock-tube problem. We use this test not only to check whether our code works properly, but also to analyse its convergency performance. The classical reference for this test is Gingold & Monaghan (1983), to whom we refer for the initial conditions of the problem. The time-steps and the smoothing lengths are constant, and fixed to 0.05 and 0.025, respectively. In other words, the smoothing lengths are set to be twice the maximum interparticle separation. The particle masses (0.003125 in our case) are obviously chosen in such a way that the density and pressure profiles are matched (Gingold & Monaghan 1983). The kernel is suitably normalized using the normalization constant $2/3h$ (see for instance Hernquist & Katz 1989).

In Fig. 1 we show the results for pressure, density, velocity and entropy of a simulation of the shock-tube problem obtained using 400 particles and both the spline and super-Gaussian kernels (right- and left-hand panels, respectively). The aim is to check whether by using different kernels it might be possible to eliminate the so-called *blip* in the pressure profile (indicated by an arrow in Fig. 1). The nature of the blip is well known, and it is the signature of the contact discontinuity in the shock. In practice the pressure is discontinuous at this point, and the corresponding smoothed value $\langle Pr \rangle$ is expected to be somewhat lower and higher at the left- and right-hand sides of the contact discontinuity, respectively (Gingold & Monaghan 1983). Even if in our simulation the shock is broadened over a $4 \times h$ region, the blip occurs as the signature of the unphysical step in the pressure.

We find that even using the super-Gaussian kernel the blip, albeit smoothed out, does not disappear. In contrast to Gingold & Monaghan (1983), we are not able to eliminate the blip even using their new formulation for the pressure force,

$$\frac{\nabla Pr}{\rho} = \rho^{\gamma-2} [\nabla (Pr\rho) + (\gamma-1) Pr \nabla \rho]. \quad (19)$$

Instead of trying other expressions for the pressure gradient, after adopting a certain combination of kernel and pressure gradient, we prefer to run simulations with a different number of particles to check whether the SPH code can eventually recover the analytical solutions when larger and larger numbers of particles are used.

In Fig. 2 we show the number, N_{blip} , of particles involved in the blip as a function of the total number of particles N_{tot} in the simulations. N_{blip} is the number of particles counted in a searching sphere of radius equal to $2 \times h$ near the blip location, and it is normalized to the total number N_{tot} . The results are as expected, in the sense that N_{blip} strongly decreases at increasing N_{tot} , or equivalently at decreasing smoothing scale. These experiments show that the blip survives because of the still-insufficient resolution.

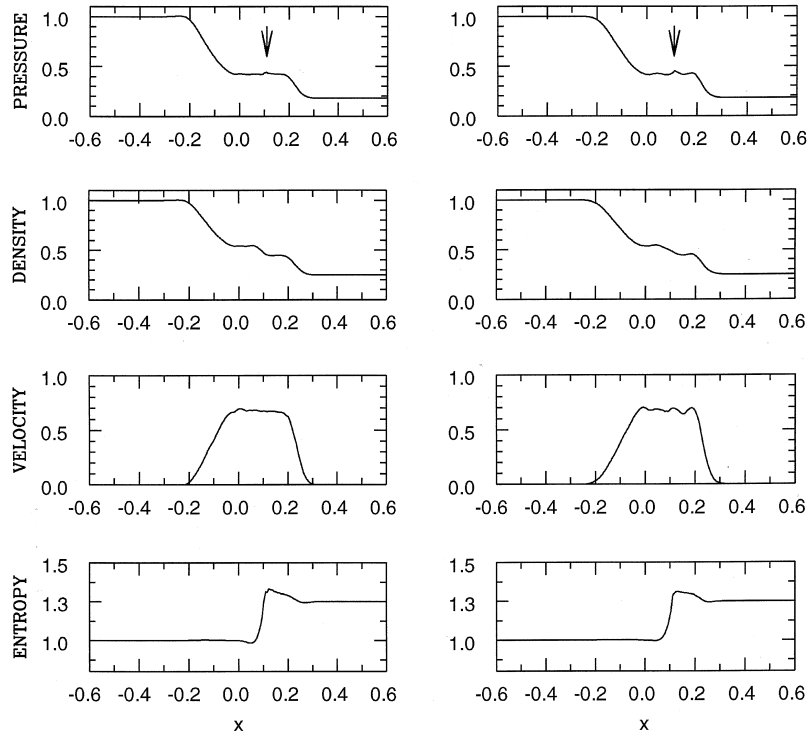


Figure 1. Result of the shock-tube problem using a super-Gaussian kernel (left-hand panel) and a spline kernel (right-hand panel). In both cases 400 particles have been used. The arrow indicates the so-called blip in the pressure profile.

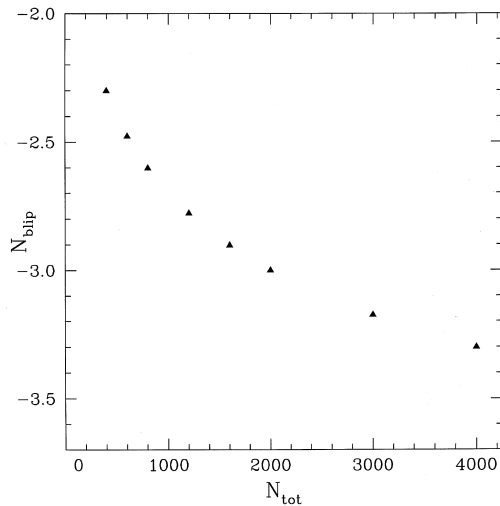


Figure 2. The number of particles involved in the blip versus the total number of particles in the simulation. N_{blip} is on a logarithmic scale.

In Fig. 3 we show the results of simulations performed using different combinations of kernels and gradient pressure terms. The region of interest is blown up for the sake of better understanding. Panel (a) is for a super-Gaussian kernel and the functional expression for $\nabla P/\rho$ by Gingold & Monaghan (1982). Panels (b) and (c) show the same but using the standard formalism for the pressure gradient, and adopting a super-Gaussian and a spline kernel, respectively. In all the three panels the blip is clearly visible.

We notice, in particular, that the first combination of

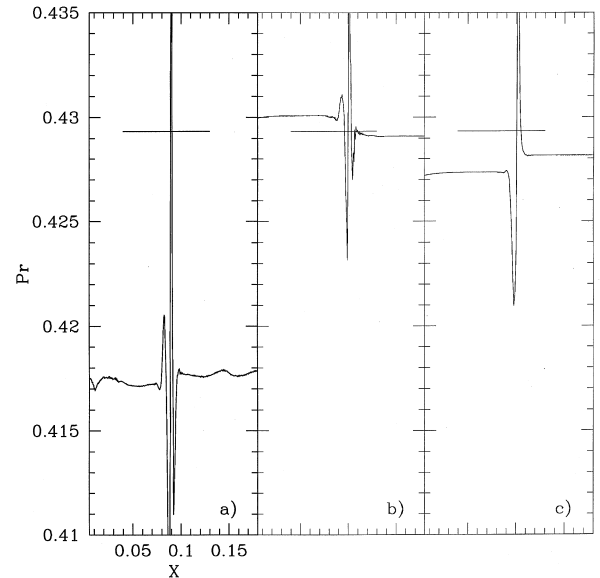


Figure 3. Blow-up of the contact discontinuity in the pressure profile. The left-hand panel (a) shows the results obtained from adopting the super-Gaussian kernel and the force term from Gingold & Monaghan (1983). The central (b) and right-hand (c) panels show the same but for standard formalism for the pressure gradient and the super-Gaussian and spline kernels, respectively. The dashed line is the analytical solution.

kernel and pressure gradient yields the best results, even if the numerical solution strongly departs from the analytical one. In the case with super-Gaussian kernel and standard pressure gradient (panel b), the step in pressure is exactly

the opposite of what is expected. Finally, in contrast to Gingold & Monaghan (1983), the inclusion of thermal conduction (cf. Lia 1996) does not eliminate the pressure step. Most likely, the blip is a feature intrinsic to the SPH smoothing itself.

As far as testing the convergency is concerned, we proceed as follows. We select four regions in the pressure profile, derive the maximum and minimum values from the numerical solutions for an increasing number of particles in the simulation, and compare them with the analytical ones. We choose the pressure as a test physical quantity because of its sensitivity to the numerical technique. The pressure, in fact, is computed from the smoothed density and energy, instead of being directly smoothed out.

The four selected regions are the undisturbed warm fluid at the left of the shock (1), two regions near the shock, to the left (2) and to the right (3), respectively, and a region just to the right of the blip (4). These regions are centred at the linear coordinate $x = -0.6$, -0.2 , $+0.04$ and $+0.2$, respectively. The particles considered in the pressure evaluation are those contained in the $2 \times h$ searching sphere.

The differences between numerical and analytical solutions are shown in Figs 4 and 5.

In Fig. 4 we show the pressure (left) and velocity (right) differences Δ between numerical and analytical solutions for an increasing number of particles in the simulation. The plotted differences are the means of their values in the four test regions. As expected, the largest differences occur in the pressure profile. The four panels of Fig. 5 show the maximum and minimum values of the pressure in the four regions at increasing total number of particles as indicated. In each panel the horizontal line shows the analytical case by definition.

All these numerical tests prove the quick convergency of the numerical solution to the analytical one, and, compared with similar experiments by other authors, show that satisfactory agreement is achieved.

Finally, we also report that the strong double-shock-tube experiment (cf. Steinmetz & Müller 1993) has also been successfully performed (Carraro 1995).

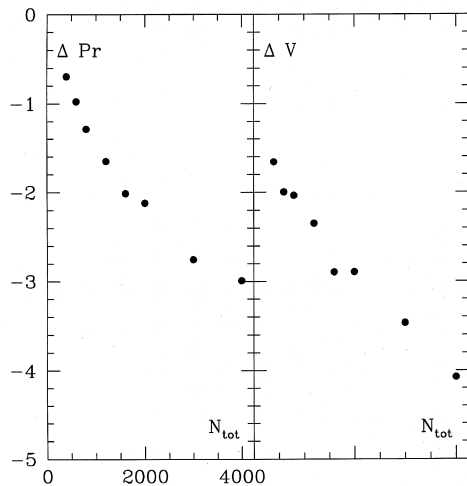


Figure 4. Convergency test. The differences Δ between the numerical and analytical solutions for pressure and velocity profiles as a function of the total number of particles in the simulation.

4 3D NUMERICAL TESTS

In three dimensions we consider the adiabatic collapse of an initially non-rotating isothermal gas sphere. This is a standard test for SPH codes (Hernquist & Katz 1989; Steinmetz & Müller 1993; Nelson & Papaloizou 1994). To facilitate the comparison of our results with those of the above authors, we adopt the same initial model and the same units ($M=R=G=1$). The system consists of a $\gamma=5/3$ gas sphere, with an initially isothermal density profile:

$$\rho(r) = \frac{M(R)}{2\pi R^2} \frac{1}{r}, \quad (20)$$

where $M(R)$ is the total mass inside the sphere of radius R . Following Evrard (1988), the profile is obtained by stretching an initially regular cubic grid by means of the radial transformation

$$r_i^{\text{old}} \Rightarrow r_i^{\text{new}} = \left(\frac{r_i^{\text{old}}}{R} \right)^3 R. \quad (21)$$

Alternatively it is possible to use the acceptance–rejection procedure of Hernquist & Katz (1989). The total number of particles used in this simulation is 2176. All the particles have the same mass. The initial specific internal energy is set to $u=0.05 GM/R$.

4.1 Gravity

In PD-SPH, the Newtonian forces are calculated using the Barnes–Hut tree-code (Barnes & Hut 1986). The tree-code is also used to perform the search of neighbours. We also include the multipole expansion, and smooth out the

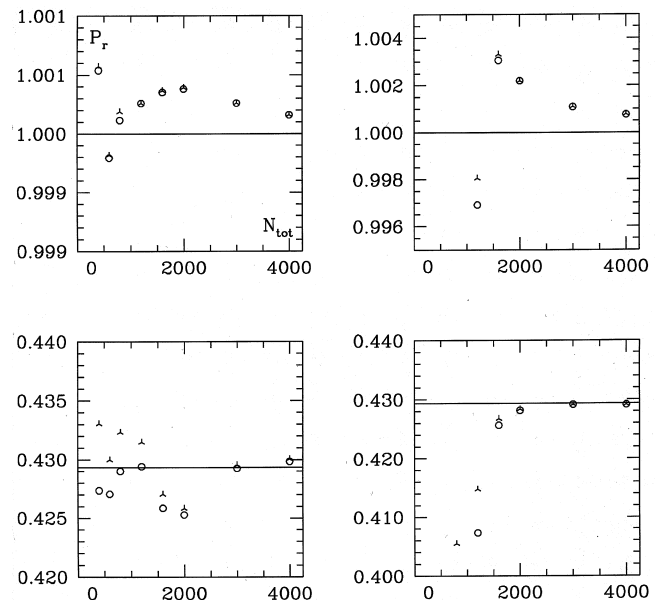


Figure 5. Convergency test. The differences Δ between the numerical and analytical solutions in each of the four regions defined in the text. Open circles and crosses are for the minimum and maximum pressure. The continuous line represents the analytical solution.

acceleration and the potential by means of the Hernquist & Katz (1989) formalism. We adopt the opening angle $\theta=0.8$, and tie the gravitational softening parameter ϵ to the particle number by looking at the mean interparticle separation at half-mass radius. In the simulations below $\epsilon \approx 0.15$.

4.2 Description of the tests

The temporal evolution of the system is shown in the various panels of Figs 6 and 7, which display the radial velocity and the specific internal energy, respectively. Each panel shows the variation of the physical quantity under consideration (in suitable units) as a function of the normalized radial coordinate at different time-steps. These (in units of the dynamical time-scale of the system) are exactly the same as in Hernquist & Katz (1989).

The initial low internal energy is not sufficient to support the gas cloud, which starts to collapse. Approximately after one dynamical time-scale a bounce occurs. The system can be described as an isothermal core plus an adiabatically expanding envelope pushed by the shock wave generated at the stage of maximum compression. After about three dynamical times the system reaches virial equilibrium with total energy equal to half of the gravitational potential energy.

The temporal evolution of the potential and kinetic energies and the total angular momentum is shown in Fig. 8. As pointed out by Nelson & Papaloizou (1994), the energy conservation, expressed as $\Delta E/E$, is ≈ 8 per cent. This uncertainty is caused by neglecting ∇h terms and using multiple time-steps. In brief, when the number of active particle becomes too small, this causes fluctuations that may affect

the energy conservation. Evolving the system with a unique time-step for all the particles lowers the uncertainty on the energy conservation down to about 5–6 per cent. As far as the angular momentum is concerned, this is conserved within 1 per cent. Going back to the panels of Figs 6 and 7, the present results agree fairly well with the mean values of the Hernquist & Katz (1989) models provided that the effects of the different numbers of particles are taken into account. For example, the shock is located at the radial

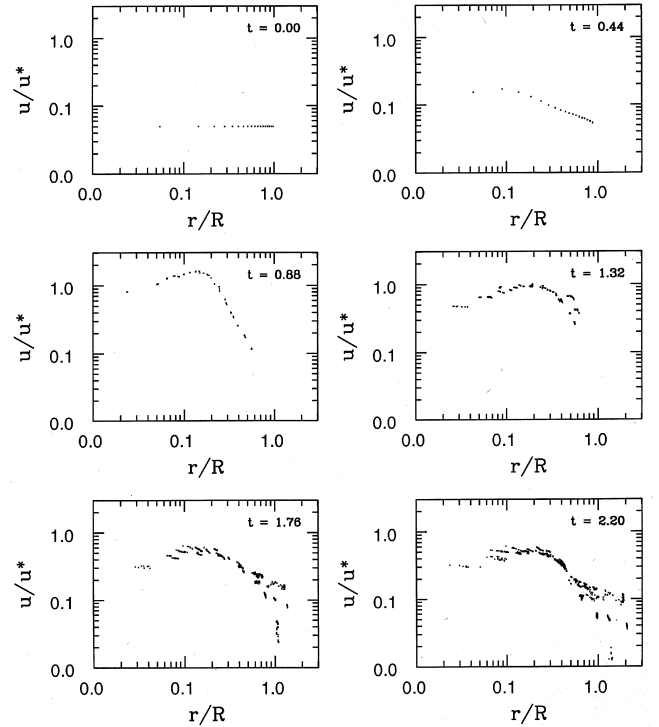


Figure 7. Adiabatic collapse: the evolution of the specific internal energy profile [in units of $u_* = GM/R$] as a function of age. The selected ages are the same as in Hernquist & Katz (1989).

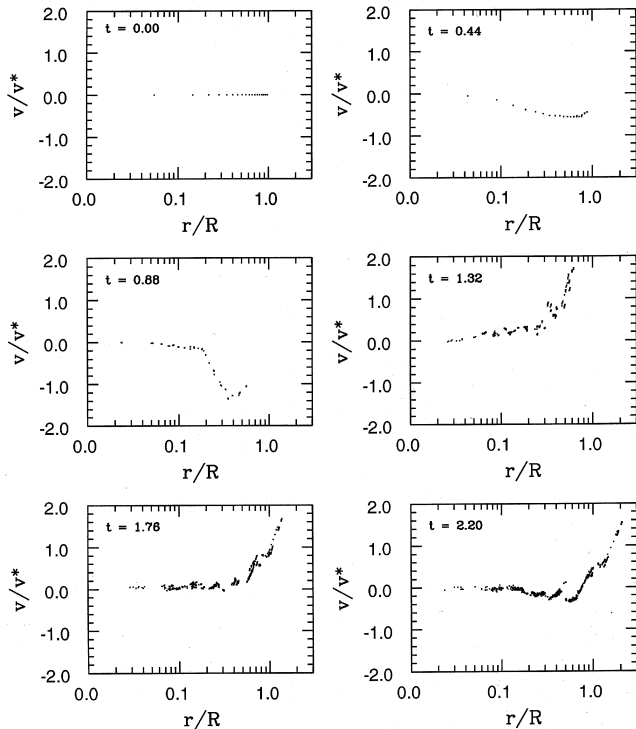


Figure 6. Adiabatic collapse: the evolution of the radial velocity profile [in units of $v_* = (GM/R^2)^{1/2}$] as a function of age. The selected ages are the same as in Hernquist & Katz (1989).

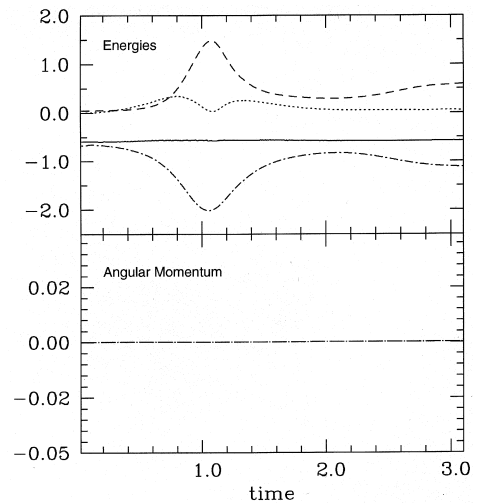


Figure 8. Adiabatic collapse. Upper panel: conservation of potential (dash-dotted line), kinetic (dotted line), thermal (dashed line), and total energy (continuous line). Lower panel: conservation of total angular momentum.

distance $0.18 \leq r/R \leq 0.25$ in the models with age $t \approx 0.88$ (cf. the velocity panels of Fig. 6). The thermal energy slowly increases for $r/R \leq 0.1$ (cf. the panels of Fig. 7). Finally, at the time of maximum compression ($t \approx 1.1$), the dynamical range in the time steps is 20:1. The scatter shown by the velocity and internal energy in the post-shock phases is caused by the relatively small number of particles, and the use of the multiple time-step scheme. Similar scatter is also present in Steinmetz & Müller (1993) and Nelson & Papanicolaou (1994).

The above numerical tests have been performed on a Digital ALPHA OSF/1 workstation. It took about 5400 seconds of CPU time for 1019 time-steps. It is worth comparing the CPU times required by different sections of our code with those of Hernquist & Katz (1989). The comparison is summarized in Table 1. It appears that the fractions of CPU time spent in key sections of our code agrees with those of the Hernquist & Katz (1989) code.

5 DARK MATTER

We consider now a collapsing cloud of gas and dark matter (DM) with initial solid-body rotation. The inclusion of dark matter is an important step, because it is known to play a key role in any modern theory of galaxy formation and evolution (cf. Frenk et al. 1996; Persic & Salucci 1997).

Initially, the dark matter particles have the same spatial distribution as the gas particles. Both in fact are obtained by stretching an initial regular cubic grid (Evrard 1988). Therefore, dark matter and gas initially obey the same density profile.

This is a source of a technical difficulty with the tree-code algorithm because when two particles occupy the same position, the tree-code is not able to distinguish between them when trying to divide the volume into elementary cells, each of which contains either only one particle or no particles at all. This difficulty does not, of course, occur with the binary tree-code algorithm (cf. Benz et al. 1989). To handle this problem within a single tree-code scheme, we force the tree-code to consider a subdivision as an elementary cell also when two particles are enclosed, provided that they are of different natures. This implies that every particle needs an additional flag specifying the species.

The system under consideration simulates a spherical galaxy with total mass and radius of $10^{12} M_{\odot}$ and 100 kpc, respectively. In addition, the system is supposed to be made of equal numbers (2176) of particles in the form of baryons and dark matter but with different individual mass such that

the total mass fraction of baryons is 0.1 times the total mass of the galaxy.

We adopt an initial solid-body rotation around the z -axis with angular velocity $\omega \approx 0.5$, which corresponds to a frequency of about 1 complete rotation in 10 free-fall time-scales, so the effects of rotation become sizeable during the collapse. This rotation corresponds to adopting the dimensionless spin parameter

$$\lambda = \frac{J|E|^{1/2}}{GM^{5/2}} = 0.08,$$

which is somewhat larger than the value expected from the tidal torque in the hierarchically clustering universe theories, i.e. $\lambda \approx 0.05$ (White 1984; Steinmetz & Bartelmann 1996).

The gravitational softening parameters ϵ for gas and dark matter are in code units (see below) 0.002 and 0.010 (200 pc and 1 kpc in physical units) respectively. They have been fixed on the basis of the Evrard (1988) relation

$$\frac{Gm}{\epsilon} \ll \frac{GM}{R}. \quad (22)$$

The parameter ϵ is kept constant in time for each individual particle. However, if in a cell two particles of different nature (gas and DM) co-exist, the softening parameter is the mass-weighted mean value.

Tests similar to those described below can be found in Navarro & White (1993) to which our results can be compared. In this context, the most salient result of the Navarro & White (1993) calculations is the different evolutionary behaviour of the dark matter and baryonic components. The same results are recovered here as shown in Figs 9 and 10, respectively. In our models, however, the difference is less pronounced because of the lower initial spin as compared to $\lambda = 0.10$ in Navarro & White (1993). In brief, dark matter has a more flattened spatial distribution than the baryonic component. In fact, equidensity contours of equal total density. It is worth recalling that observational hints for flatter dark haloes have been found in galaxies like NGC 5907 (Sackett et al. 1994), NGC 4244 (Olling 1996), and NGC 891 (Becquaert & Combes 1997).

6 NON-ADIABATIC PROCESSES

As far as the evolution of the gaseous component is concerned, all non-adiabatic processes except artificial viscosity are of paramount importance. In fact, they drive the energy and momentum loss or gain of these 'particles'. As the final target is to follow the evolution of a real galaxy, processes like cooling and heating, star formation and feedback play a dominant role, and must be included from the very beginning in order to obtain results worth comparing with observational data. Unfortunately, some of these processes are not yet well understood. The physics of star formation, in particular, is far from being assessed so that parametrizations of this basic process are imposed.

In this section we present in some detail our assumptions concerning thermal conduction and cooling processes of the gaseous component, which are known to regulate the

Table 1. CPU time percentage in the adiabatic collapse.

Section of the code	Hernquist & Katz	This work
Gravitational computation	43.28	42.63
SPH computation	27.63	26.37
Search of the nearest neighbors	24.43	26.22
Tree construction	4.50	4.28
Miscellaneous	0.16	0.50

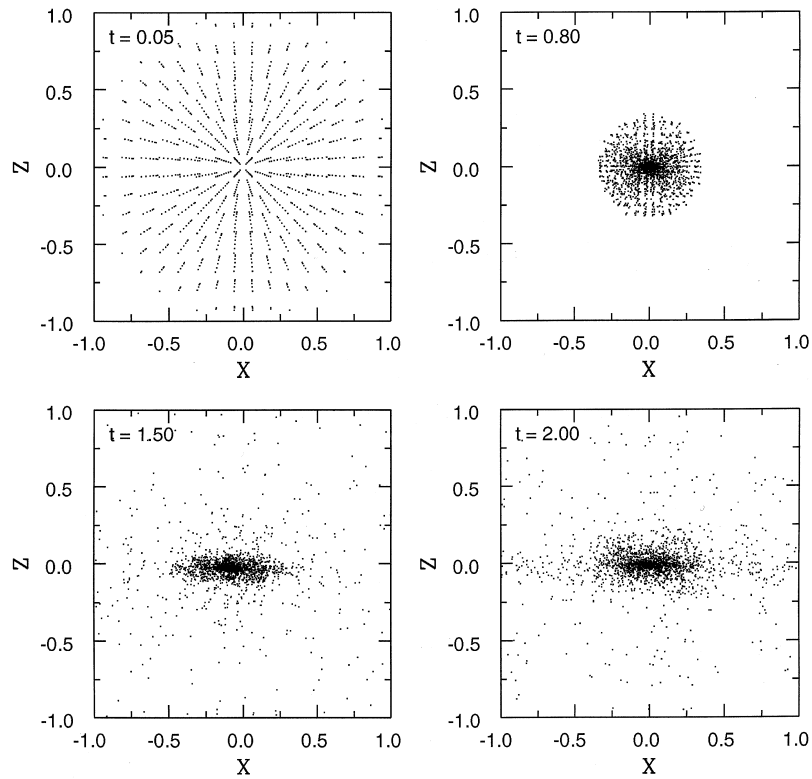


Figure 9. Adiabatic collapse: the evolution of the dark matter component as a function of time in the x - z plane. Time is in code units.

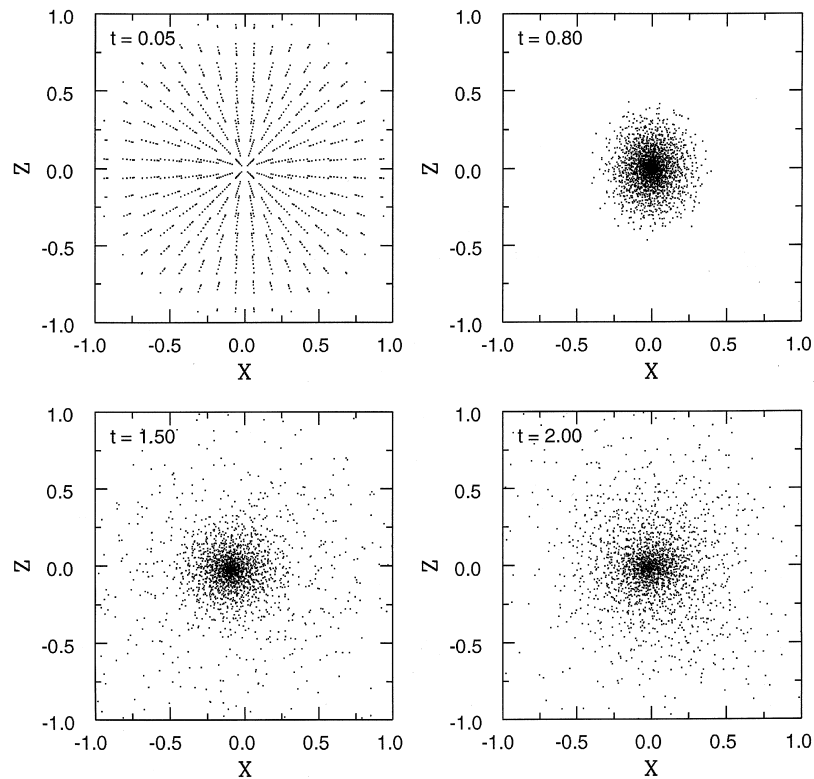


Figure 10. Adiabatic collapse: the evolution of the baryonic component as a function of time in the x - z plane. Time is in code units.

energy budget of a fluid element. They are included in the energy equation as source terms.

6.1 Thermal conduction

Thermal conduction is calculated according to the formalism developed by Monaghan & Lattanzio (1991):

$$\frac{1}{\rho} \nabla \cdot (\rho q \nabla u). \quad (23)$$

The translation of it into the SPH language is

$$\sum_{j=1}^N m_j \frac{(q_i = q) (u_i - u_j) \mathbf{r}_{ij} \cdot \nabla W(\mathbf{r}_{ij}, h)}{\rho_{ij} (r_{ij}^2 + \eta^2)}, \quad (24)$$

where q is the thermal conductivity function. This is in turn evaluated as

$$q_i + q_j = gh(c_{ij} - 4 \cdot \mu_{ij}), \quad (25)$$

In the above relations, η is a parameter ensuring that the denominator of relation (25) remains different from zero, and g is another suitable parameter set equal to 0.25.

Thermal conduction is expected to be effective in situations of strong shocks, and/or ‘wall heating’, when two flows or two fluid elements collide. Thermal conduction is a source of heating in the energy equation (see below).

6.2 Cooling

Radiative cooling is the crucial mechanism responsible for the condensation and collapse of baryonic gas into galaxies and, inside galaxies, for the occurrence of star formation. Cooling processes are rather well known, and have already been included in current models of galaxy formation and evolution, albeit in different detail. See for instance Katz, Weinberg & Hernquist (1996) for a very accurate treatment of cooling processes of different natures. Among the various cooling agents we recall (i) the radiative cooling by atomic and molecular processes, and (ii) the inverse Compton mechanism in the presence of microwave background radiation.

6.2.1 Radiative cooling

The most commonly used radiative cooling functions are those by Katz & Gunn (1991) because they are analytical and continuous with their first derivatives. These radiative cooling functions are calculated assuming the typical helium abundance by mass $Y=0.25$. They do not contain, however, the dependence on metallicity which, in contrast, is expected to be important during the evolution of a galaxy, as a natural consequence of the chemical enrichment. To cope with this drawback of the Katz & Gunn (1991) cooling functions, we adopt here those elaborated by Chiosi et al. (1997). In brief, these cooling functions $\Lambda_c(u_i, \rho_i, Z_i)$ are derived from literature data, and include different radiative processes. For temperatures greater than 10^4 K they lean on the Sutherland & Dopita (1993) tabulations for a plasma under equilibrium conditions and metal abundances $[\text{Fe}/\text{H}] = -10$ (no metals), -3 , -2 , -1.5 , -1 , -0.5 , 0 (solar) and 0.5 . For temperatures in the range $100 \leq T \leq 10^4$ the

dominant source of cooling is the H_2 molecule becoming rotationally or vibrationally excited through a collision with an H atom or another H_2 molecule and decaying through radiative emission. The data in use have been derived from the analytical expressions of Hollenbach & McKee (1979) and Tegmark et al. (1996). Finally, for temperatures lower than 100 K, starting from the relation of Theis et al. (1992) and Caimmi & Secco (1986), Sutherland & Dopita incorporate the results of Hollenbach & McKee (1979) and Hollenbach (1988) for CO as the dominant coolant. The following analytical relation in which the mean fractionary abundance of CO is given as a function of $[\text{Fe}/\text{H}]$ is found to represent the normalized cooling rate well (i.e. $\Lambda_c(\text{CO})/n^2$ with n the number density of particles):

$$\Lambda_c(\text{CO}) = 1.6 \times 10^{-29} 10^{([\text{Fe}/\text{H}] - 1.699)} T^{0.5} \text{ erg cm}^3 \text{ s}^{-1}. \quad (26)$$

The normalized cooling rate (in units of $\text{erg cm}^3 \text{ s}^{-1}$) over the whole temperature range is shown in Fig. 11, in which the effects of the metallicity are clearly visible. It is worth mentioning that no rescaling of the cooling rate from the various sources has been applied to obtain the smooth curves shown in Fig. 11. For the purposes of comparison, we display in Fig. 11 the cooling rate of Katz & Gunn (1991). The major point of disagreement is soon evident, because their cooling rate which by definition is for a zero-metal composition actually lies well above the zero-metal curve of Sutherland & Dopita (1993). This implies that Katz & Gunn’s (1991) cooling is unphysically more efficient in situations of nearly zero metallicity, such as the protogalactic phase.

6.2.2 Inverse Compton cooling

We do not take into account inverse Compton cooling because of its strong dependence on redshift. During the photogalactic phase of the evolution of a galaxy, from which we start our simulations, the inverse Compton cooling has

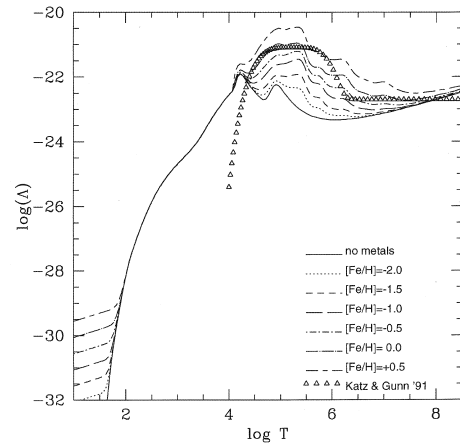


Figure 11. Net cooling rate Λ_c/n^2 in $\text{erg cm}^{-3} \text{ s}^{-1}$ as a function of temperature. n is the number density of particles. The cooling rate is from Sutherland & Dopita (1993) for $T \geq 10^4$ K, Hollenbach & McKee (1979) and Tegmark et al. (1996) for $100 \leq T \leq 10^4$ K, and Caimmi & Secco (1986) and Theis et al. (1992) for $T \leq 100$ K. Each curve corresponds to a different metallicity as indicated. For comparison the cooling rate by Katz & Gunn (1991) is superposed (open triangles).

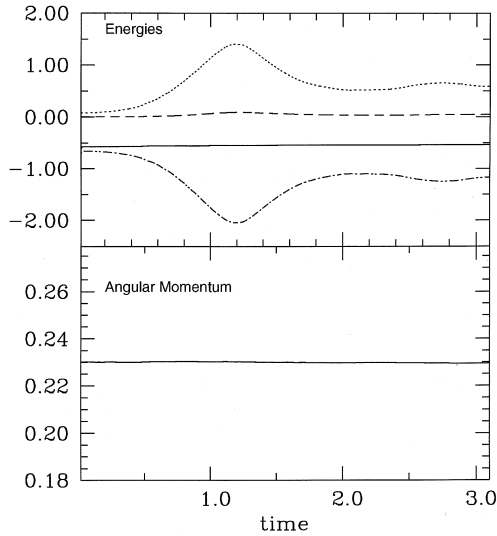


Figure 12. Collapse of a clump of gas and dark matter. Upper panel: conservation of potential (dashed–dotted line), kinetic (dotted line), thermal (dashed line) and total energy (continuous line). Lower panel: conservation of total angular momentum.

already become much lower than the radiative cooling, so that it can be neglected.

Although the cooling rate has been derived over a wide range of temperatures from a few degrees to above 10^8 K, in reality only the portion above a suitable temperature T_{\min} can be used in model calculations because of the maximum resolution achievable in the N -body simulations. This limit is derived from imposing that the Jeans mass does not fall below a critical value, which is conventionally assumed to be the mass of four gas particles (cf. Katz & Gunn 1991). The limit temperature is given by the Bonnor–Ebert expression (Ebert 1955; Bonnor 1956)

$$T_{\min} = 0.89553 \left[\left(\frac{4m_p}{\rho_g} \right)^{2/3} - \left(\frac{\pi \epsilon_g^3}{3} \right)^{2/3} \right] \frac{\mu m_H G}{k} \rho_g, \quad (27)$$

where m_p is the mass of a baryonic particle, k is the Boltzmann constant, and μ and ϵ are the mean molecular weight and the gas gravitational softening parameter, respectively.

The limit temperature T_{\min} is locally computed for every gas particle. Finally, the cooling functions are stored in the code as look-up tables.

6.3 Heating

Heating of the gas is caused by many processes, among which we consider the thermalization of the energy deposit by supernova explosions (both Type I and II), stellar winds from massive stars, the ultraviolet flux from massive stars, the cosmic ultraviolet flux, and finally sources of mechanical nature.

6.3.1 Supernovae

The rate of supernova explosions $R_{\text{SNI,II}}(t)$ over the time interval Δt is calculated according to standard prescriptions

[cf. Bressan et al. 1994; Tantalò et al. 1996, 1997; Greggio & Renzini 1983 for Type I supernovae (SNe) in particular]. Knowing the amount of energy released by each SN explosion, the total energy injection over the time interval Δt is the sum of two terms, E_{SNI} and $E_{\text{SNI,II}}$, of type

$$E_{\text{SNI,II}} = \int_{\Delta t} \epsilon_{\text{SNI,II}} R_{\text{SNI,II}}(t') dt', \quad (28)$$

where $R_{\text{SNI,II}}(t)$ is the number of supernovae per unit time, and $\epsilon_{\text{SNI,II}}$ is the energy injected per SN explosion. This formulation slightly differs from the one commonly adopted in chemical models of galaxies, in which $\epsilon_{\text{DNI,II}}(t)$ is the thermalization law of SDN remnants including the cooling processes (cf. Bressan et al. 1994; Tantalò et al. 1996). In our scheme, first cooling effects are left to the energy budget equation; secondly owing to the limitations implicit in the N -body technique we are not yet able to resolve the star-forming fluid to the level of individual stars but only to that of massive cluster-like structures in which stars can be formed according to a given initial mass function (see below). Therefore, following in detail the thermalization law of SNe is impossible. A reasonable compromise is obtained by using sufficiently small time-steps (cf. also Chiosi et al. 1997 for a similar approach). The explicit formulations for $R_{\text{SNI,III}}(t)$ will be presented in the next section.

6.3.2 Stellar winds

The rate of energy injection by stellar winds is

$$E_w = \int_{\Delta t} \epsilon_w R_w(t') dt', \quad (29)$$

where R_w is the number of stars per unit time expelling their envelopes during the time interval Δt and, analogy with the SN remnants, ϵ_w is the kinetic energy of stellar winds. A star that loses mass is expected to deposit into the interstellar medium the energy

$$\epsilon_{w0} = \eta \times \frac{M_{\text{ej}}(M)}{2} \left(\frac{Z}{Z_\odot} \right)^{0.75} \times v(M)^2, \quad (30)$$

where $M_{\text{ej}}(M)$ is the amount of mass ejected by each star of mass M , $v(M)$ is the velocity of the ejected material, and η is an efficiency factor of the order of 0.3. The calculation of the rate $R_w(t)$ is postponed to the next section.

6.3.3 Ultraviolet flux from massive stars

The rate of energy injection from the ultraviolet flux emitted by massive stars is

$$E_{\text{UV}} = \int_{\Delta t} \epsilon_{\text{UV}} R_{\text{UV}}(t') dt', \quad (31)$$

where R_{UV} is the number of massive stars per unit time the mass of which is the range 10 – $20 M_\odot$, and ϵ_{UV} is the amount of ultraviolet energy emitted by each star. To calculate ϵ_{UV} the following procedure is adopted. We suppose that massive stars are located on the zero-age main sequence, i.e.

obeying well-known mass–luminosity–effective temperature relationships, $LL_{\odot}(MM_{\odot})$ and $T_{\text{eff}}(MM_{\odot})$. In principle, there should be an additional dependence on the chemical composition which, however, can be neglected here. The relationships $LL_{\odot}(MM_{\odot})$ and $T_{\text{eff}}(MM_{\odot})$ are taken from the library of stellar models/isochrones of Bertelli et al. (1994 and references therein). For the sake of simplicity we can approximate the spectral energy distribution of any such stars as pure blackbody emission of given T_{eff} , for which we can immediately estimate the fraction $F_{\text{UV}}(M)$ of flux emitted shortward of 4000 Å (our range for UV light) by a star of mass M . The UV flux emitted by each star is

$$\epsilon_{\text{UV}} = F_{\text{UV}}(M) \times L(M), \quad (32)$$

where L is the total luminosity of the star. Once again the calculation of $R_{\text{UV}}(t)$ is postponed to the next section.

6.3.4 Cosmic UV radiation

As far as the UV radiation field is concerned, its effects have been thoroughly investigated by Navarro & Steinmetz (1996) who reached the conclusion that the cosmic UV radiation plays some role only when the gas has already accreted on to the protogalaxy from the surrounding medium. Heating by cosmic UV radiation is not included in the present models. In this context, it is worth recalling that all models in which the cosmic UV radiation is the sole source of heating face the so-called *overcooling* problem (cf. Navarro & Steinmetz 1996).

6.3.5 Total radiative heating

The total heating rate resulting from radiative processes $H_{\text{R}}(u, \rho, Z)$ to be included in the energy budget equation (see below) is

$$H_{\text{R}} = \frac{E_{\text{SNI}} + E_{\text{SNII}} + E_{\text{W}} + E_{\text{UV}}}{\Delta t}. \quad (33)$$

6.3.6 Mechanical heating

In principle there are various mechanical processes that contribute to heat gas particles. Two of them have been explicitly taken into account in the basic energy equation (8). They have been referred to in short form as Γ_{LM} and are generally functions of type $\Gamma_{\text{LM}}(u, \rho, Z)$.

6.4 More details on the energy equation

At this stage of the analysis we can write down the detailed expression of the energy equation in all its components. To this aim we need only to convert the radiative heating into the conventional SPH formalism

$$\Gamma_{\text{R},i}(u, \rho, Z) = \sum_j H_{\text{R},j} \times \frac{m_j}{\rho_j} W(i, j) \quad (34)$$

with obvious meaning of the symbols. The final energy equation is

$$\frac{du_i}{dt} = \Gamma_{\text{M},i} + \Gamma_{\text{R},i}(u, \rho, Z) - \frac{\Lambda_{\text{C},i}(u, \rho, Z)}{\rho_i} \quad (35)$$

with

$$\Gamma_{\text{R},i}(u, \rho, Z) = H_{\text{C},i}(u, \rho, Z) + H_{\text{R},i}(u, \rho, Z), \quad (36)$$

where $\Gamma_{\text{R},i}$ is the sum of thermal conductivity and all radiative heating sources. The energy u_i is per unit mass, whereas all other quantities are per unit mass and time.

The functional dependence of the cooling term imposes an implicit solution of the energy equation. This is performed using hybrid scheme, i.e. a combination of the Newton–Raphson and bisection methods. The associated second-order updating of the thermal energy follows the technique of Hernquist & Katz (1989).

Finally, it is worth mentioning that under high cooling efficiency situations can be met in which the energy may become negative. To cope with this unphysical result of mere numerical nature we impose that a gas particle cannot lose more than half of its thermal energy per time-step (Hernquist & Katz 1989).

7 TESTING COOLING PRESCRIPTIONS

In this section we show an ideal galactic model in which no star formation, no chemical enrichment and no energy deposit from the various sources are allowed to occur. This model is meant to show the net results of different prescriptions for the cooling rate. The model has zero metal content and, apart from the cooling rate, it is identical to that by Katz & Gunn (1991) so that the comparison is possible.

We simulate the collapse of a spherical galaxy with mass of $10^{12} M_{\odot}$ and radius of 100 kpc. As in the previous test, the baryon fraction is 0.1, while the initial gas temperature is 10^4 K. In this simulation, time, spatial coordinates, energy and density are expressed in the following units: [time] = 7.41×10^8 yr, [space] = 100 kpc, [energy] = 4.30×10^{14} erg g^{-1} and [density] = 1.61×10^{-25} g cm^{-3} . The temporal evolution of the models has been followed up to the age of 2.2 dynamical times (approx. 1.6 Gyr).

The results are schematically presented in Figs 13 and 14. Fig. 13 shows the distribution of particles on the x – z plane at three different ages (in code units) for our cooling rate (left-hand panels) and Katz & Gunn (1991) (right-hand panels), whereas Fig. 14 compares the cooling radiation for the two assumptions for the cooling rate.

As the zero-metal cooling rate of Sutherland & Dopita (1993), on which our prescription stands for temperatures above 10^4 K, is much less efficient than that of Katz & Gunn (1991), this easily explains why significantly longer time-scales are needed to form disc structures (cf. Fig. 13), and the much lower amount of radiated energy (cf. Fig. 14).

Finally, in Fig. 15 we show the conservation of total energy and angular momentum as a function of time for the case with the new cooling rate. The small decrease of the total energy with increasing time is caused by the loss of thermal energy radiated away by cooling processes (for comparison see the detailed trend of energies in Fig. 11). Angular momentum is conserved within 5 per cent accuracy (see also Fig. 11 for comparison).

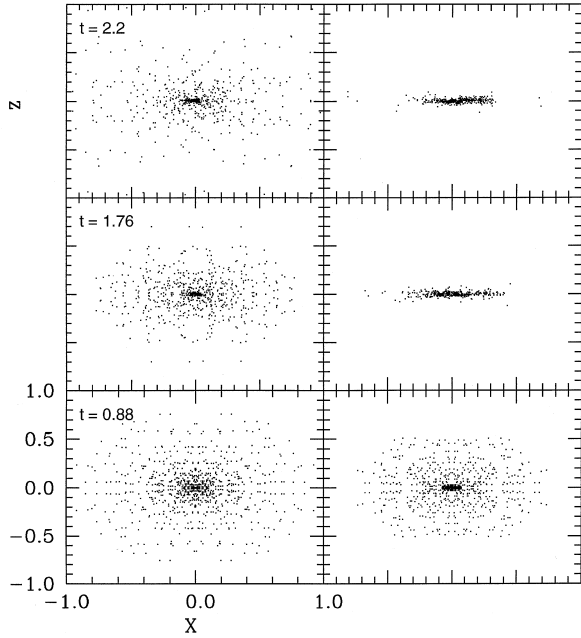


Figure 13. Testing cooling: the final distribution in the x - z plane for gas particles in simulations with different cooling prescriptions. The right-hand panel is for the cooling rate by Katz & Gunn (1991), whereas the left-hand panel is for the cooling prescription described in the text.

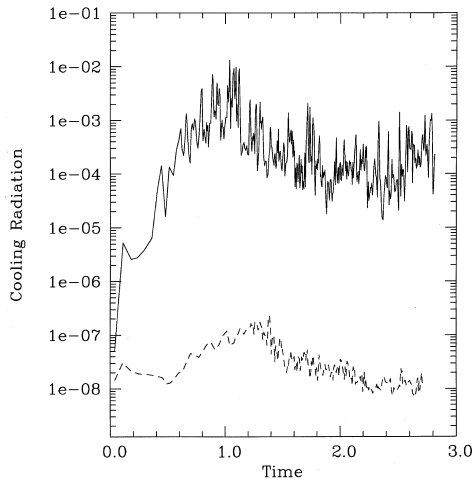


Figure 14. Cooling radiation (in code units): the solid line is for the cooling rate by Katz & Gunn (1991), whereas the dashed line is for the cooling rate used in this paper.

8 GOING TOWARD COMPLETE MODELS: STAR FORMATION, FEEDBACK AND CHEMICAL ENRICHMENT

Implementing star formation into N -body simulations of galaxies is a cumbersome affair, reflecting partly our poor knowledge of this fundamental process, and partly the limitations still imposed by the N -body technique itself.

To accomplish the task, two basic steps are required: first we need to determine the star-formation rate (SFR), and

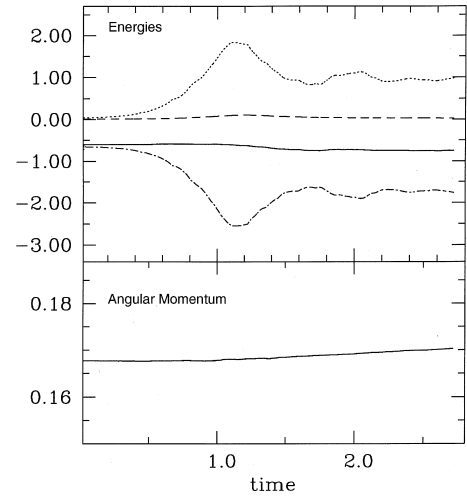


Figure 15. Conservation of energy and angular momentum in a collapsing galaxy with the cooling rate adopted in this paper. The model is the same as in the left-hand panel of Fig. 13.

secondly we must treat the effects of the star formation on the interstellar medium (the so-called feedback).

8.1 Star-formation rate

To include star formation in the N -body scheme two important pieces of information are needed: first we have to set suitable conditions under which stars can form, and secondly we must express the SFR law governing the efficiency at which gas is turned into stars (cf. Stainmetz 1995 for a review on the subject).

8.1.1 When to form stars?

There are at least three physical conditions to be met in order to activate the star-forming process. First, a fluid element is eligible to make stars if it is part of a convergent flow, i.e. the particle velocity divergence must satisfy the condition

$$\nabla \cdot \mathbf{v}_i < 0. \quad (37)$$

Secondly, the fluid element must be Jeans unstable:

$$\frac{h_i}{c_i} > \frac{1}{\sqrt{4\pi G \rho_i}}. \quad (38)$$

Finally, the gas particle must remain cool:

$$\tau_{\text{cool}} \leq \tau_{\text{ff}}. \quad (39)$$

This last condition is usually translated into an overdensity criterion. For instance, Navarro & White (1993) use the following expression:

$$\rho_i > \rho_{\text{crit}}, \quad (40)$$

where $\rho_{\text{crit}} = 7 \times 10^{-26} \text{ g cm}^{-3}$. This minimum threshold density actually holds only in the case of a single cooling function (no dependence on chemical composition). However, as star formation causes metal enrichment of the interstellar medium, the threshold moves towards lower values

at increasing metallicity. Because of this, we prefer to adopt condition (39) which is of general validity.

8.1.2 Star-formation law

A very popular, empirically based, rate of star formation is the Schmidt (1959) law, according to which

$$\Psi(t) = \frac{d\rho_{\text{gas}}}{dt} = -\frac{d\rho_{\text{star}}}{dt} = c_* \frac{\rho_{\text{gas}}}{\tau_{\text{ff}}}, \quad (41)$$

where c_* is the specific efficiency (in most cases a free parameter).

In dense regions (the ones prone to star formation), the cooling time τ_{cool} is typically much shorter than the dynamical time τ_{ff} . As $\tau_{\text{ff}} \propto \rho_{\text{gas}}^{-1/2}$, the SFR is proportional to $\rho_{\text{gas}}^{3/2}$, a result that agrees with Schmidt's (1959) observational estimates. In most numerical simulations, the specific efficiency is taken to be $c_* = 0.1$.

8.2 Star-like particles

When star formation has started, at any time-step Δt a star-like particle is created, the mass of which is

$$m_* = m_{\text{gas}} \times \left[1 - \exp\left(-\frac{c_* \Delta t}{\tau_{\text{ff}}}\right) \right], \quad (42)$$

and the mass of the parent gas particle is consequently reduced. The above relation simply follows from integrating equation (41) over the time-step Δt . The mass of the star-like particles obviously depends on the resolution (number of particles) of the simulation.

The star-like particle is supposed not to immediately acquire its own individuality, but to leave the parent gas particle only when the mass of the latter falls below a certain value (typically 50 per cent of the original mass). Furthermore, recurrent episodes of star formation within the same gas particle are possible, so that gas is depleted in discrete steps. Finally, the star-like particle is treated as a collisionless object. Therefore, the element of fluid in which star formation occurs is considered as a hybrid particle, the collisional component of which experiences both hydrodynamical and gravitational forces, while its collisionless component feels only the gravitational field.

To avoid non-physical accelerations caused by the sudden decrease of the gas mass, particles in which star formation is active are stored in the lowest time-bin.

When a star-like particle leaves its parent, it inherits its position in phase space and its gravitational softening parameter. Resolution limitations force us to consider only four star-formation events per gas particle, as Navarro & White (1993).

8.3 Feedback

To qualitatively evaluate the feedback by all heating processes already outlined in the previous section, we need to know the initial mass function (IMF), according to which the newly born stars will distribute by number in each mass interval dM . For the sake of simplicity we adopt here the classical Salpeter (1955) law:

$$\Phi(M) dM = A \cdot M^{-x} dM, \quad (43)$$

where $x=2.35$ (the Salpeter value) and A is the normalization constant. This is derived from imposing that stars can be formed with masses in the range $0.1-120 M_{\odot}$, and assuming that the integral of equation (43) over this mass range is equal to 1. It is worth recalling that only stars more massive than about $0.9 M_{\odot}$ will be able to pollute the interstellar medium over a time-scale shorter than the Hubble time (cf. Tinsley 1980; Matteucci 1997). The normalization constant is $A=0.06$. Other IMFs are already implemented into the code (Miller & Scalo 1979).

8.3.1 Supernova rates

In the standard scenario of stellar evolution (cf. Greggio & Renzini 1983), Type II supernovae occur in single stars more massive than say $8 M_{\odot}$, whereas Type I (more precisely Ia) supernovae occur in binary stars containing a rejuvenated white dwarf brought to explosion via the C-deflagration mechanism by mass accretion from the companion. Furthermore, Type II supernovae from progenitors more massive than say $30 M_{\odot}$ leave behind a black hole (scarcely contributing to the enrichment of the interstellar medium in heavy elements), whereas Type II supernovae from progenitors in the mass range 8 to $30 M_{\odot}$ leave a neutron star and most effectively contribute to chemical enrichment in heavy elements. Type I supernovae have binary-system progenitors with typical total mass in the range 3 to $16 M_{\odot}$.

To evaluate the rate of Type I occurrence, one has to know the percentage of binary systems with respect to single stars. Let C be this fraction. Following Greggio & Renzini (1983), the rate of Type I supernovae is

$$R_{\text{SNI}} = C \int_{M_{\text{B,inf}}}^{M_{\text{B,max}}} \Phi_{\text{B}}(M_{\text{B}}) dM_{\text{B}} \times \int_{\mu_{\text{inf}}}^{1/2} 2^{\gamma+1} (1+\gamma) \mu^{\gamma} \Psi[t - t_{(\mu, M_{\text{B}})}] d\mu. \quad (44)$$

In the above expression M_{B} is the total mass of the binary system, $\Phi_{\text{B}}(M_{\text{B}})$ is the IMF of binary stars, which is assumed here to be the same as for single stars (equation 43) for the sake of simplicity, $\mu = M_2/M_{\text{B}}$ is the fractionary mass of the secondary, which drives the evolution, and γ is a coefficient, usually equal to 2. Finally, $M_{\text{B,inf}}$ and $M_{\text{B,max}}$ are the lower and upper limits for the total mass of the binary stars, respectively, and μ_{inf} is the lower limit for the fractionary mass of the secondary. These masses are calculated with the following receipt:

$$M_{\text{B,inf}} = \max(2M_2, 2) \quad (45)$$

$$M_{\text{B,max}} = 8 + M_2, \quad (46)$$

$$\mu_{\text{inf}} = \max[M_2(t)/M_{\text{B}}, 1/2]. \quad (47)$$

Finally, $\Psi(t)$ is the SFR at the time equal to the difference between the current time and the lifetime of M_2 .

The total rate of Type II supernovae is

$$R_{\text{SNII}} = \int_{M_{\text{B,max}}}^{120} \Phi(M) \Psi(t_{\text{M}}) dM$$

$$+ (1 - C) \int_8^{M_{B, \max}} \Phi(M) \Psi(t_M) dM, \quad (48)$$

with obvious meaning of the symbols.

Finally, the constant C above is calibrated by looking at the rate of Type Ia supernovae in spiral galaxies (van den Bergh & McClure 1994). C turns out to be ≈ 0.04048 . The contribution by supernovae explosions to feedback has also been included in the TREE-SPH model of the Milky Way by Raiteri, Villata & Navarro (1996).

8.3.2 Stellar winds and UV fluxes

The rates R_W and R_{UV} , i.e. the number of stars per unit mass and time contributing to the energy injection by stellar winds and UV flux, are simply given by

$$R_W = R_{UV} = \int_{10}^{120} \Phi(M) \Psi(t_M) dM. \quad (49)$$

All mass–lifetime relationships entering the above calculations of the rates $R_{SNI, II}$, R_W and R_{UV} are derived from the library of stellar models/isochrones of Bertelli et al. (1994). Whenever possible the effect of the chemical composition of the fluid element is taken into account.

8.3.3 Final remark

Each supernova explosion produces 10^{51} erg of energy, which is injected into the interstellar medium in the form of kinetic energy. A comparable amount of energy is supplied by a massive star during its whole lifetime in the form of stellar wind. In the case of supernovae, only a small fraction of this energy is thermal (a few per cent), and this small fraction is immediately (100 yr is the typical time-scale) radiated away, for instance in the form of X-ray emission. The effect of this energy input on the velocity field of the surrounding medium is expected to be negligible. In brief, while the typical space resolution of current simulations is about 1 kpc or more, supernova shocks may affect volumes of about 100 pc radius around the exploding star (Mazzali & Cappellaro, private communication). Therefore it is not possible to follow the dynamics of such explosions down to the required resolution. On the basis of these considerations, the claim that some fraction of the supernova energy budget (10^{-4} or so of the total) can modify the velocity field of the neighbouring volumes of our star-like particles is not solidly grounded. We prefer to simply assume that the cumulative effect of the supernova explosions increases the mean temperature and internal energy of the gas on a scale larger than the size of a fluid element.

8.4 Chemical evolution

In our simulations, the chemical enrichment of the interstellar medium follows the prescriptions of Steinmetz & Müller (1994). It stands on the closed-box, instantaneous recycling description (cf. Tinsley 1980), i.e. the metal abundance Z of a fluid element is computed as

$$\Delta Z_i = - Y_Z \frac{\Delta m_{i, \text{gas}}}{m_{i, \text{gas}}}, \quad (50)$$

where Y_Z is the so-called yield per stellar generation. Given a certain stellar nucleosynthesis scenario (cf. Matteucci 1997), Y_Z can be calculated a priori in a way mutually consistent with the assumed IMF. Using the results of chemical models by Portinari et al. (1997), a good assumption for yield per stellar generation is $Y_Z = 0.005$.

Once metals are synthesized, they are spread according to the SPH formalism:

$$\langle Z_i \rangle = \sum_{j=1}^N Z_j \frac{m_j}{\rho_j} W(R_{ij}, h). \quad (51)$$

Groom (1997) suggests that the chemical enrichment of the interstellar medium is better described by the diffusive equation

$$\frac{dZ}{dt} = -\kappa \Delta^2 Z, \quad (52)$$

where Z is the metallicity and κ the diffusion coefficient, with κ equal to $50 \text{ km s}^{-1} 60 \text{ pc}$. The SPH translation, which requires second derivatives of the kernel, is

$$\frac{dZ_i}{dt} = - \sum_{j=1}^N \kappa m_j \left(\frac{2}{\pi_j + \rho_j} \right) (Z_i - Z_j) |\nabla^2 W_{ij}(|\mathbf{r}_i - \mathbf{r}_j|, j_j)|. \quad (53)$$

Chemical enrichment is expected to occur on the same spatial scale as the energy release of supernova explosions, i.e. about 100 pc, which is much smaller than the spatial resolution of our model.

Although the use of the second derivative of the smoothing function may introduce spurious fluctuation in the resulting metallicity implicit in equation (55), this is less of a problem as far as the global enrichment in metals is concerned.

In fact, in semi-analytical models of chemical evolution of disc-like galaxies (Tinsley 1980; Carraro, Ng & Portinari 1997; Portinari et al. 1997 and references therein) the metallicity is known quickly to reach the metallicity yield of the contributing stellar population.

Therefore we expect that the result does not critically depend on the particular scheme used to evaluate the metallicity variation with the SPH method. This is implicitly confirmed by the agreement between theoretical results and observational data for the solar vicinity that are presented in the section below.

We have adopted equation (55), and converted the metallicity Z to $[\text{Fe}/\text{H}]$ by means of the relation

$$[\text{Fe}/\text{H}] = \log(Z) + 1.739 \quad (54)$$

taken from Bertelli et al. (1994).

9 THE CASE OF A DISC-LIKE GALAXY

The code described in the previous section has been used to study the formation and evolution of disc-like galaxies. The initial model consists of a $10^{12} M_\odot$ spherical galaxy enclosed within a radius $R = 100 \text{ kpc}$ and containing 1000 particles of baryonic mass and 1000 particles of dark matter. We have assumed that the fractionary total mass of baryons is 0.1 times the total mass of the galaxy and the spin parameter $\lambda = 0.08$, which is in the range of current estimates for disc galaxies.

9.1 No feedback

In Figs 16 and 17 we show the dynamical evolution of a disc-like galaxy in the absence of feedback. Under the combined action of rotation and cooling, gas settles on to a disc (cf. left-hand panels of Figs 16 and 17) and stars start to be formed. Remarkably, at the age of about 5 Gyr a bulge-like structure made of stars is observed, whereas a disc-like structure is not yet visible because of insufficient resolution, and our assumption that stars are considered as such when the gas fraction of each star-forming unit has fallen below 0.5 times the total mass. We expect the disc to appear at higher ages. Like the case of the collapsing galaxy without cooling and star formation, a flattened halo of dark matter can develop (cf. the central panels of Figs 16 and 17 and Fig. 9). Another important result of the new cooling rate is that gas particles survive in the halo for significantly large periods of time.

The temporal evolution of the star formation and supernova rates is shown in Fig. 18. As expected, the rate of star formation is low and nearly constant with time. Furthermore, while Type II SNe closely follow the trend of the star formation, Type I SNe appear in significant proportions only later than about 1.5 Gyr because of the rather long lifetime of their progenitors. Finally, in Fig. 19 we show the age–metallicity relation for the gas component in the disc of the galaxy and compare it with the age–metallicity relation for disc stars in the solar vicinity by Edvardsson et al. (1993). Despite the crudeness of our modelling of chemical enrichment,

the agreement is remarkable, in particular at ages higher than 2 Gyr, when the metallicity has saturated to the yield.

9.2 Complete feedback

The spatial evolution of the disc-like galaxy in the presence of full feedback is shown in Figs 20 and 21, which display the gas (left-hand panels), dark matter (central panels) and star particles (right-hand panels) at three different ages, namely 0.5 (bottom), 2.5 (middle) and 5 Gyr (top). As expected, the galaxy remains less spatially concentrated owing to the energy input from the various sources and consequent heating. This is particularly true for the gas and star particles, whereas no sizeable effect is seen on the dark matter component. The rates of star formation and Type I and II supernova explosions as a function of time are shown in the three panels of Fig. 22. Although the global trend is as in the previous case, now the three rates are down by approximately a factor of 2. This can be easily understood as a result of heating, which keeps the system less spatially concentrated (lower density), thus immediately lowering the rate of star formation and supernova explosions in turn.

In Fig. 23, we show the age–metallicity relation for the gas component on the disc of the galaxy and compare it with the age–metallicity relation for disc stars in the solar vicinity by Edvardsson et al. (1993). The same remark made on Fig. 9 still applies.

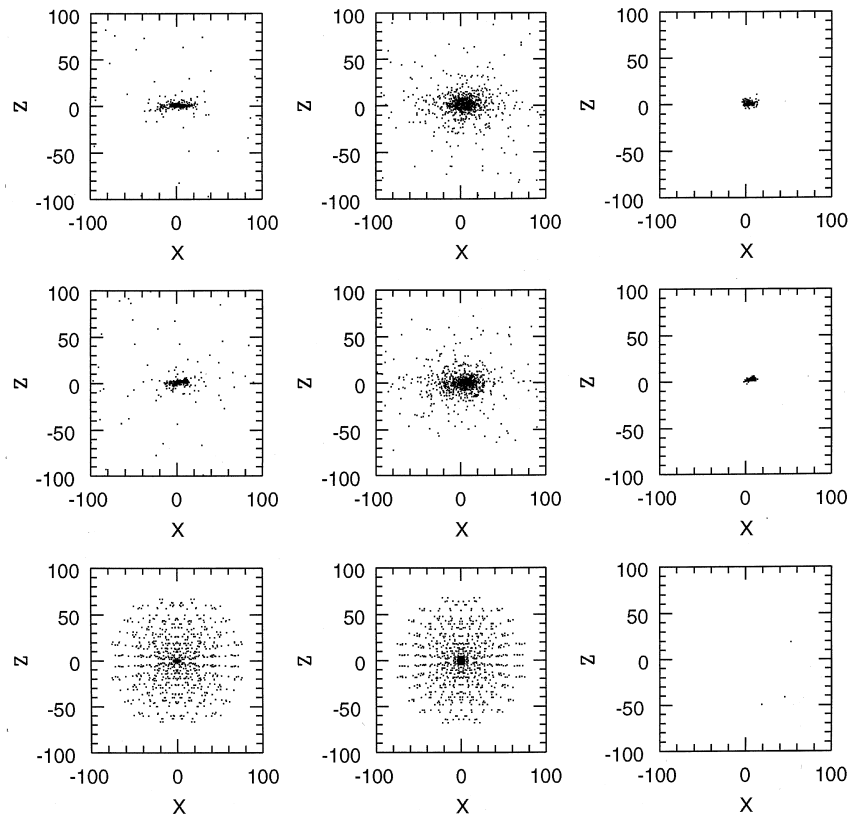


Figure 16. Simulation of a disc-like galaxy with no feedback: the spatial distributions of gas (left-hand panel), dark matter (central panel) and stars (right-hand panel). Starting from the bottom, the three panels of each row refer to ages of 0.5, 2.5 and 5 Gyr.

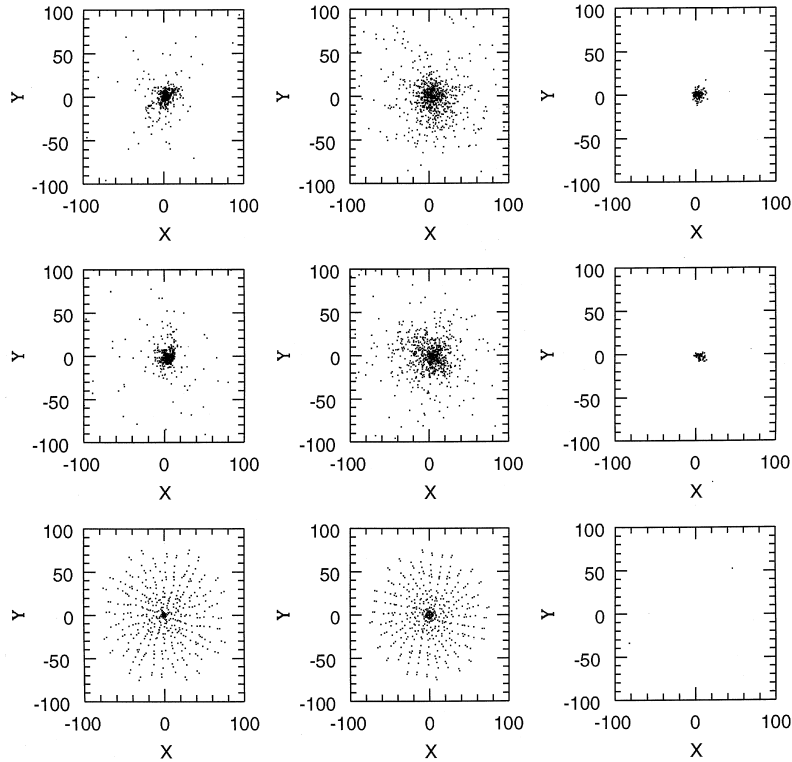


Figure 17. Simulation of a disc-like galaxy with no feedback: the same as in Fig. 16 but on to the x - y plane.

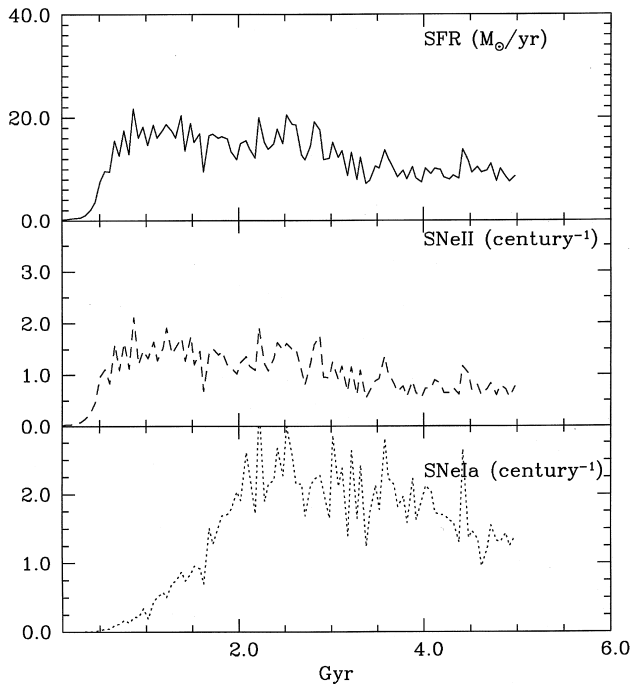


Figure 18. Simulation of a disc-like galaxy with no feedback: the rates of star formation (top panel) and supernova explosions (Type II: middle panel, Type I: bottom panel).

Finally, in order to prove that the mean density of the two model galaxies is actually different, we plot in Fig. 24 the ratio $m_{\text{gas}}/(m_{\text{gas}} + m_{\text{stars}})$ as a function of age. The dashed line is the galaxy with no feedback at all, whereas the solid line is for the galaxy with full feedback.

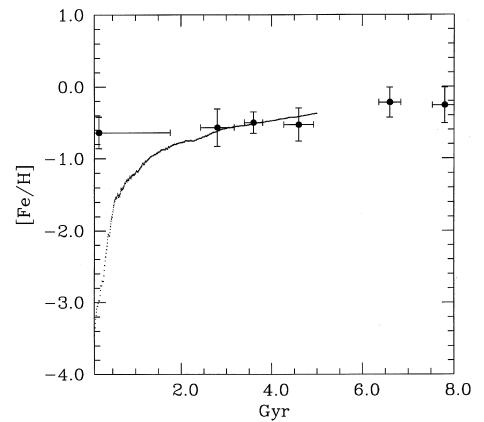


Figure 19. Simulation of a disc-like galaxy with no feedback: the age-metallicity relation for the gas component in the galactic disc. Filled circles show the age-metallicity relation of disc stars in the solar vicinity by Edvardsson et al. (1993).

10 CONCLUSIONS AND FUTURE PERSPECTIVES

In this paper, we have presented a new TREE-SPH code suited to studies of the formation and evolution of galaxies.

Particular attention has been paid to including modern descriptions of non-adiabatic processes, such as cooling and heating by supernova explosions, stellar winds and UV radiation from massive stars, so that feedback in the energy balance is not a parameter but naturally follows from the assumed star-formation rate and initial mass function. Fur-

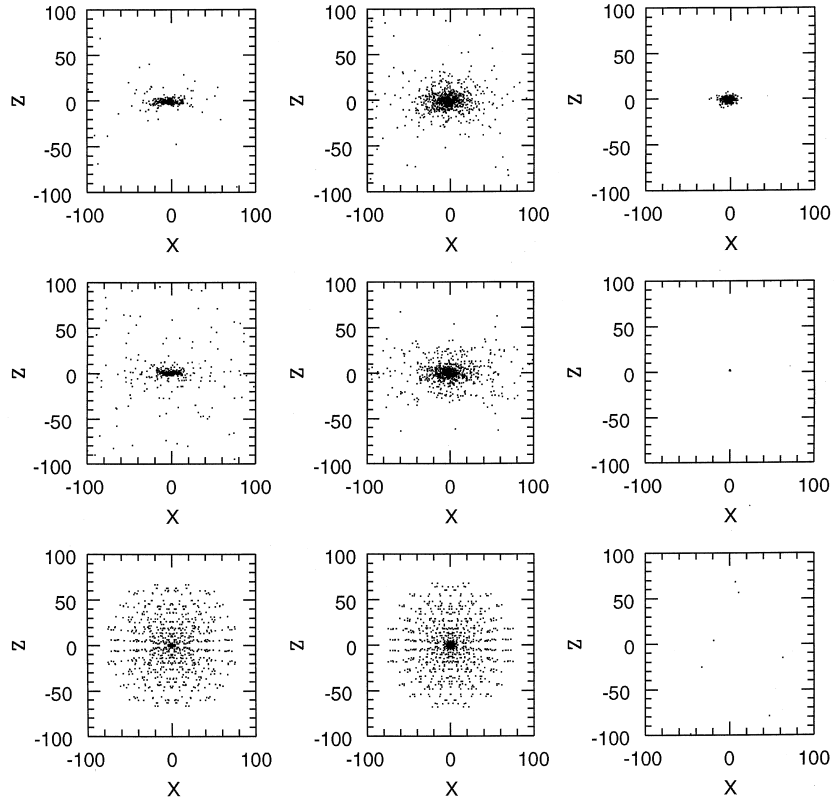


Figure 20. Simulation of a disc-like galaxy with full feedback: the spatial distribution of gas (left-hand panel), dark matter (central panel) and stars (right-hand panel). Starting from the bottom, the three panels of each row refer to ages of 0.5, 2.5 and 5 Gy.

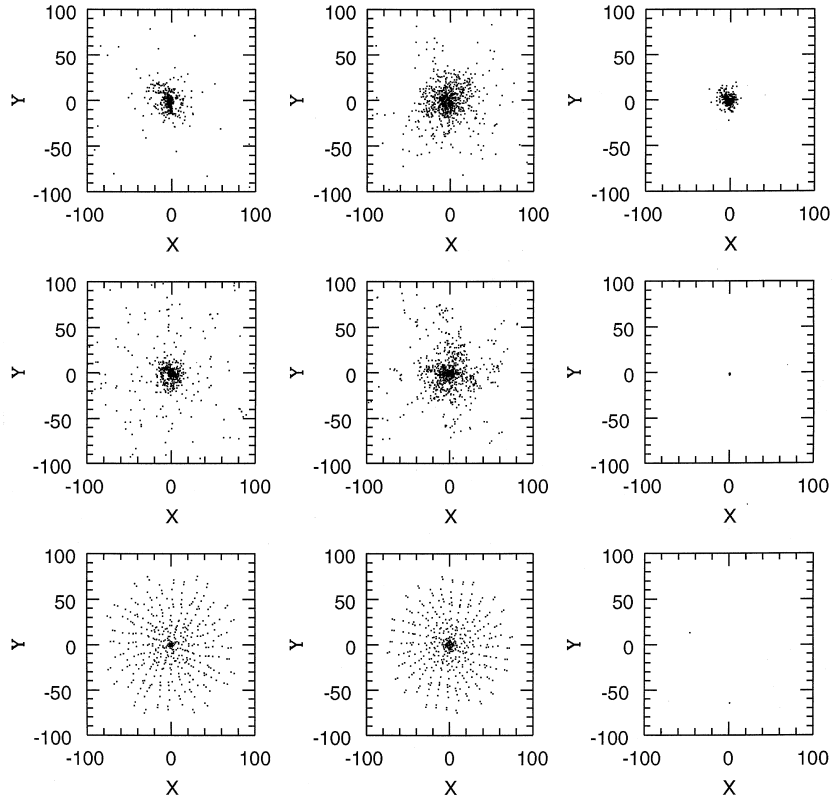


Figure 21. Simulation of a disc-like galaxy with full feedback: the same as in Fig. 20 but on to the x - y plane.

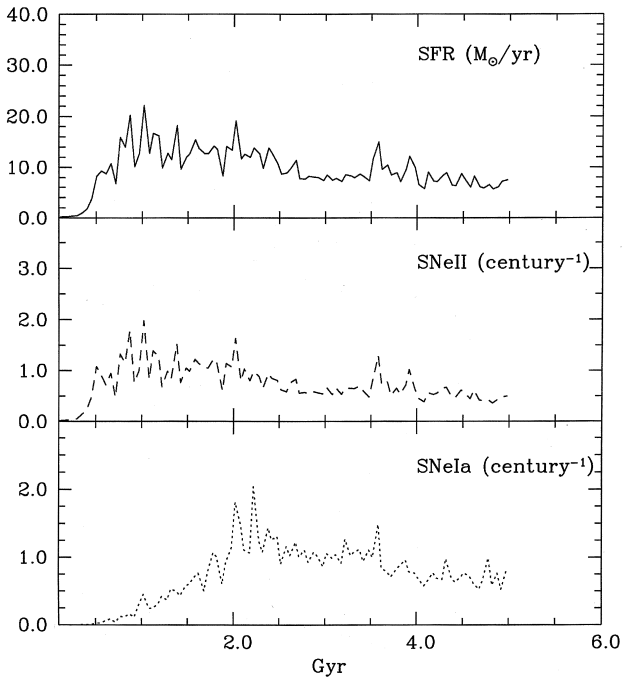


Figure 22. Simulation of a disc-like galaxy with full feedback: the rates of star formation (top panel) and supernova explosions (Type II: middle panel, Type I: bottom panel).

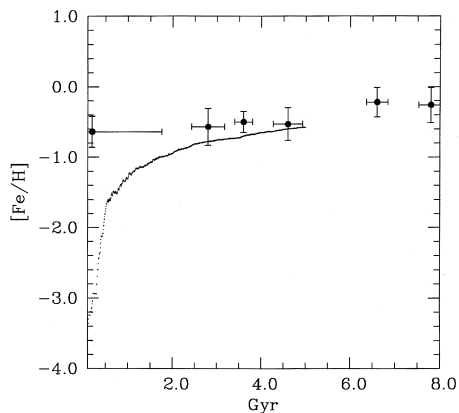


Figure 23. Simulation of a disc-like galaxy with full feedback: the age–metallicity relation for the gas component of the galactic disc. Filled circles show the age–metallicity relation for disc stars in the solar vicinity by Edvardsson et al. (1993).

thermore, we have followed the chemical enrichment of gas as the consequence of star formation and include the dependence of the cooling rate on the gas chemical composition (metallicity). These are points of major difference and improvement with respect to similar codes in the literature.

Although the initial conditions are not tuned to any specific cosmological scenario, the ones we have adopted still lead to reasonable results. This point will be the subject of future improvements.

In addition to many classical tests aimed at checking the performance of the code and its response to different physical assumptions, we have presented the results for two disc-

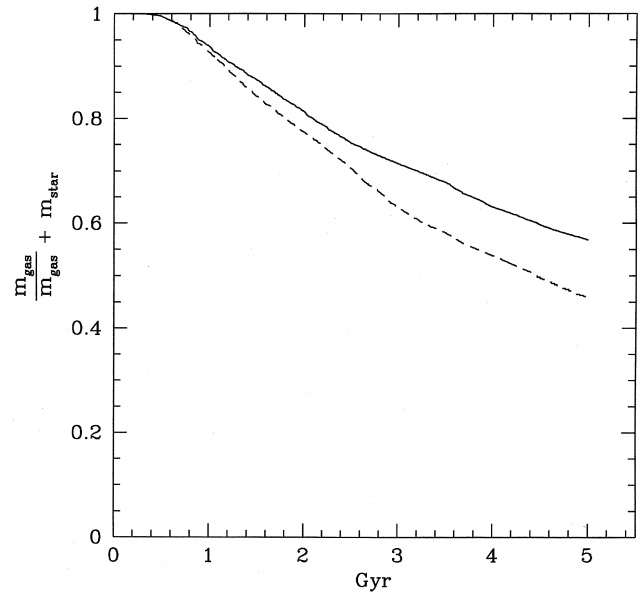


Figure 24. The gas fraction in models with no feedback (dashed line) and full feed-back (solid line).

like galaxies with and without feedback for the purposes of comparison, both internal and with similar studies in the literature.

Particularly relevant is the role played by the dependence of the cooling rate on the chemical composition (metallicity), which owing to its strong impact on the final results can no longer be neglected in simulations of galaxy formation and evolution.

Work is in progress to extend these models to the case of elliptical galaxies and to build the proper interface between this code and the spectrophotometric code of Bressan et al. (1994) so that the spatial history of integrated spectra, magnitudes, colours, line-strength indices, etc., can be derived together with the dynamical history for galaxies of different morphological type.

ACKNOWLEDGMENTS

GC especially thanks W. Hillebrandt, S. White, E. Müller and M. Steinmetz of the Max-Planck-Institute für Astrophysik in Garching for their warm hospitality and support during the six-month visit that made it possible to start their project. GC and CL thank L. Danese, M. Persic, P. Salucci and R. Valdarini for encouragement and many useful conversations during the year spent at ISAS, Trieste, which made it possible to continue this project. This study has been financially supported by ANTARES, the Italian Ministry of University, Scientific Research and Technology (MURST), and the Italian Space Agency (ASI). Finally, this study is part of the scientific programme ‘Galaxy formation and evolution’ financed by the European Community with the TMR grant ERBFMRX-CT96-0086.

REFERENCES

- Arimoto N., Yoshii Y., 1987, *A&A*, 173, 23
 Arimoto N., Yoshii Y., 1989, *A&A*, 224, 361

- Balsara D. S., 1995, *J. Chem. Phys.*, 121, 357
 Barnes J., Hut P., 1986, *Nat*, 324, 446
 Baugh C. M., Cole S., Frenk C. S., 1996, *MNRAS*, 283, 1361
 Becquaert J. F., Combes F., 1997, *A&A*, 325, 41
 Bender R., 1997, in Arnaboldi M., Da Costa G. S., Saha P., eds, *Proc. Second Stromlo Symposium, The Nature of Elliptical Galaxies*, in press
 Benincà M., Carraro G., 1995, in *Science and Supercomputing at CINECA, Report 1995*, 27
 Benz W., 1990, in Buchler J. R., ed., *Numerical Modelling of Nonlinear Stellar Pulsation*. Kluwer, Dordrecht, p. 269
 Benz W., Bowers R. L., Cameron A. G. W., Press W. H., 1989, *ApJ*, 348, 650
 Bertelli G., Bressan A., Chiosi C., Fagotto F., Nasi E., 1994, *A&AS*, 106, 275
 Bonnor W. B., 1956, *MNRAS*, 116, 351
 Bressan A., Chiosi C., Fagotto F., 1994, *ApJS*, 94, 63
 Bressan A., Chiosi C., Tantalo R., 1996, *A&A*, 311, 425
 Bruzual G., Charlot S., 1993, *ApJ*, 405, 538
 Caimmi R., Secco L., 1986, *Ap&SS*, 119, 315
 Carraro G., 1995, PhD thesis, Padova University
 Carraro G., Ng Y. K., Portinari L., 1997, *MNRAS*, in press (astro-ph/9707185)
 Chiosi C., Bressan A., Portinari L., Tantalo R., 1997, *A&A*, submitted (astro-ph/9708123)
 Davis M., Efstathiou G., Frenk C. S., White S. D. M., 1992, *Nat*, 356, 489
 Ebert R., 1955, *Z. Astrophys.*, 37, 217
 Edvardsson B. et al., 1993, *A&A*, 275, 101
 Evrard A. E., 1988, *MNRAS*, 235, 911
 Frenk C. S., Baugh C. M., Cole S., Lacey C. G., 1997, in Persic M., Salucci P., eds, *Dark Matter 1996: Dark and Visible Matter in Galaxies and Cosmological Implications*, p. 98
 Gibson B. K., 1996a, *ApJ*, 468, 167
 Gibson B. K., 1996b, *ApJ*, 468, 167
 Gibson B. K., 1996c, *MNRAS*, 278, 829
 Gibson B. K., Matteucci F., 1997, *ApJ*, 475, 47
 Gingold A. A., Monaghan J. J., 1983, *J. Comput. Phys.*, 46, 429
 Greggio L., Renzini A., 1983, *A&A*, 118, 217
 Groom W., 1997, PhD thesis, Univ. Cambridge
 Haehnelt M., Steinmetz M., Rauch M., 1996a, *ApJ*, 465, L95
 Haehnelt M., Steinmetz M., Rauch M., 1996b, *MNRAS*, in press
 Hernquist L., Katz N., 1989, *ApJS*, 70, 419
 Hollenbach D., 1988, *Astro. Lett. Commun.*, 26, 191
 Hollenbach D., McKee C. F., 1979, *ApJS*, 41, 555
 Katz N., 1992, *ApJ*, 391, 502
 Katz N., Gunn J., 1991, *ApJ*, 377, 365
 Katz N., Weinberg M., Hernquist L., 1996, *ApJS*, 105, 19
 Kauffmann G., White S. D. M., Guiderdoni B., 1993, *MNRAS*, 264, 201
 Kauffmann G., Charlot S., White S. D. M., 1996, *MNRAS*, 283, L117
 Lia C., 1996, Master thesis, Padova University
 Matteucci F., 1997, *Fund. Cosmic Phys.*, in press
 Miller G. E., Scalo F. J. M., 1979, *ApJS*, 41, 513
 Monaghan J. J., Lattanzio J. C., 1985, *A&A*, 149, 135
 Monaghan J. J., Lattanzio J. C., 1991, *ApJ*, 375, 177
 Navarro J. F., Steinmetz M., 1997, *ApJ*, 478, 13
 Navarro J. F., White S. D. M., 1993, *MNRAS*, 254, 271
 Navarro J. F., Frenk C. S., White S. D. M., 1996, *ApJ*, 462, 563
 Nelson R. P., Papaloizou J. C. B., 1994, *MNRAS*, 270, 1
 Olling P. R., 1996, *AJ*, 112, 481
 Persic M., Salucci P., 1997, in *Proc. Sesto conference, Dark Matter in Galaxies*
 Portinari L., Chiosi C., Bressan A., 1996, *A&A*, in press
 Raiteri C. M., Villata M., Navarro J. F., 1996, *A&A*, 315, 105
 Rampazzo R., Longhetti M., Bressan A., Chiosi C., 1997, preprint
 Sackett P. D., Morrison H. L., Harding P., Boroson T. A., 1994, *Nat*, 370, 441
 Salpeter E. E., 1955, *ApJ*, 121, 161
 Schmidt M., 1995, *ApJ*, 129, 243
 Schweizer F., Seitzer P., 1992, *AJ*, 104, 1039
 Steinmetz M., 1996a, *Proc. Int. School of Physics 'Enrico Fermi' – Dark Matter in the Universe (Varenna, Italy, 1995 July 24–August 4. IOP, Bristol)*
 Steinmetz M., 1996b, *MNRAS*, 278, 1005
 Steinmetz M., Bartelmann M., 1996, *MNRAS*, 272, 570
 Steinmetz M., Müller E., 1993, *A&A*, 268, 391
 Steinmetz M., Müller E., 1994, *A&A*, 281, L97
 Steinmetz M., Müller E., 1995, *MNRAS*, 276, 459
 Sutherland R. S., Dopita M. A., 1993, *ApJS*, 88, 253
 Tantalo R., Chiosi C., Bressan A., Fagotto F., 1996, *A&A*, 311, 361
 Tantalo R., Bressan A., Chiosi C., Portinari L., 1997, *A&A*, in press
 Tegmark M., Silk J., Rees M. J., Blanchard A., Abel T., Palla F., 1996, *ApJ*, in press
 Theis Ch., Burkert A., Hensler G., 1992, *A&A*, 265, 465
 Tinsley B. M., 1980, *ApJ*, 241, 41
 van den Bergh S., McClure R. D., 1994, *ApJ*, 425, 205
 White S. D. M., 1984, *ApJ*, 286, 38
 Worthey G., 1994, *ApJS*, 95, 107